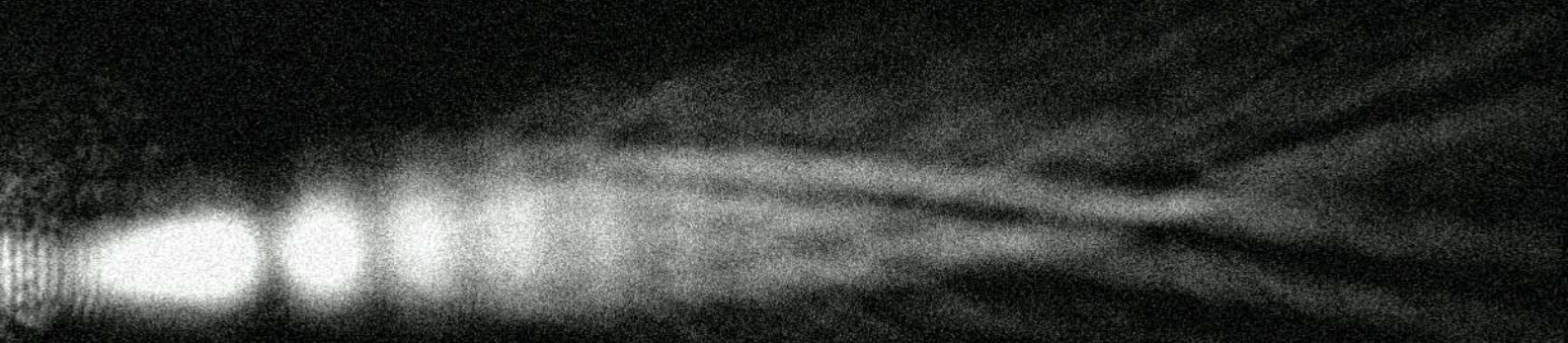


Scattering of Surface Plasmon Polaritons by Gold Nanoparticles



**University of Aalborg, 2007
Jeppe Nørgaard and René Petersen**

Title:

Scattering of Surface Plasmon Polaritons
by Gold Nanoparticles

Project Periode:

P7, 1/9-07 - 20/12-07

Project Group:

Nano, Gr. N7.210

Groupmembers:

Jeppe Mørch Nørgaard

René Petersen

Supervisor:

Sergey Bozhevolnyi
Ilya Radko

Number of Copies: 6

Number of Pages: 60

Number of Appendices: 2

Total Number of Pages: 66

Synopsis:

In this project the scattering of surface plasmon polaritons (SPPs) on gold surfaces by gold nanoparticles is treated theoretically and experimentally. Two theoretical models are developed, a scalar model and a vectorial model and it is shown that in a certain limit the two models correspond to each other. The vectorial model is based on the Greens tensor formalism. The main focus of the project is focusing of SPP beams by parabolic chains of nanoparticles but other structures are investigated theoretically as well. Excitation of SPPs in the Kretschmann-Raether configuration is tried out experimentally and the conditions for minimum reflection intensity are discussed. It is shown that the reflection intensity can be well described using Fresnel theory. The focusing of SPPs by parabolic chains of nanoparticles are investigated experimentally and theoretically and it is shown that the model corresponds well to the experiments.

Preface

This report is the product of the 7th semester project, at Aalborg University. It is written by group N7.210 consisting of two nanotechnology students, studying on the nanophysics and nanomaterials graduate studies. Associated with courses in advanced quantum mechanics, optoelectronics, failures and fractures in nanostructures, and nanomaterial chemistry, the report constitutes the 7th semester.

References are devised according to the Harvard method, listing author and publication year in edged brackets. The alphabetic reference list can be found in the back of the report. References placed in the end of a section refer to the whole section, if placed inside a sentence they only refer to the specific sentence. The following abbreviations are used as references throughout the report. Eqn.: equation, Fig.: figure, Tbl.: table, Chp.: Chapter, Sec.: Section, App.: appendix.

Vectors are written as \mathbf{A} and matrices as $\hat{\mathbf{A}}$. Inverse trigonometric functions are written as $\arcsin \theta$.

Contents

1	Introduction	9
1.1	Surface Plasmon Polaritons	9
1.2	SPP based Microprocessors	10
1.3	Focusing of SPPs	10
1.4	Leakage Radiation Microscopy	10
1.5	Biosensors	11
1.6	Purpose of the Project	12
2	Theory	13
2.1	Physics of SPPs	13
2.1.1	SPP Dispersion Relation	14
2.1.2	Excitation of SPP	17
2.1.3	Quantitative Description of Minimum Reflected Intensity	19
2.1.4	Attenuated Total Reflection - ATR	20
2.1.5	Spatial Extension and Propagation Length of SPPs	21
2.2	Scalar Model	23
2.3	Single Particle Scattering	25
2.4	Vectorial Model	26
2.4.1	Two Dipole Resonance	28
2.4.2	Near Field of a Dipole	30
2.4.3	Indirect Propagator	31
2.4.4	Relation to Surface Plasmon Polaritons	33
2.4.5	Connection to Scalar Model	34
2.4.6	In Plane Scattering of SPPs	35
3	Numerical Results	39
3.1	Scalar Model Results	39
3.1.1	Single Particle Scattering	39

CONTENTS

3.1.2	Mirrors	40
3.1.3	Waveguides	40
3.2	Vectorial Model Results	41
3.2.1	Scalar Model and Vectorial Model Comparison	42
3.2.2	Parabolic Nanoparticle Chains for SPP Beam Focusing	43
4	Experimental Setup	47
4.1	ATR Setup	47
4.2	LRM Setup	48
5	Experimental Results and Discussion	51
5.1	ATR Results	51
5.1.1	Data Fitting	52
5.2	LRM Results	53
5.2.1	Propagation Length	55
5.2.2	Parabola Shape and Particle Spacing	56
5.2.3	Shape of the SPP Beam	57
5.2.4	Comparison Between Numerical Results and Experiments	57
6	Conclusion	59
A	Surface Plasmon Excitation	61
A.1	61
A.2	61
B	Reflectivity of a two interface system	63

Chapter 1

Introduction

Contents

1.1	Surface Plasmon Polaritons	9
1.2	SPP based Microprocessors	10
1.3	Focusing of SPPs	10
1.4	Leakage Radiation Microscopy	10
1.5	Biosensors	11
1.6	Purpose of the Project	12

This chapter introduces some physical aspects of surface plasmon polaritons, SPPs, and discusses their usability as the foundation in optical computers. Methods for focusing SPPs and mapping their fields are described. In the end of the chapter the purpose of the project is explained.

1.1 Surface Plasmon Polaritons

A plasmon is a quasiparticle resulting from a collective oscillation in the charge density of a material. Plasmons can only exist in materials which support these collective oscillations. If a photon couples to a plasmon on the surface of a conductor, a surface plasmon polariton (SPP) results. This is an electromagnetic wave that propagates along the surface of a conductor with fields decaying exponentially away from the surface. It is not possible to directly couple a photon and an SPP since the photon carries too small a momentum. There are different ways to enhance the photon momentum and thereby overcome this problem. One way to do so is to use attenuated total reflection experiments devised by [Otto, 1968] and [Kretschmann and Raether, 1968]. These methods are still being used today for surface characterization and measuring of the optical constants of metals.

SPP propagation is highly sensitive to surface properties such as coating material and surface defects. To control the propagation of SPPs, metal surfaces can be designed to guide and focus SPPs for specific purposes. In the past few years nanofabrication techniques have improved and it has become possible to control the shape and composition of a surface down to nanometer sizes. Fabrication tools such as electron-beam lithography and nano-optical characterization tools such as near-field optical microscopy has increased the interest for SPPs. [Barnes et al., 2003]

1.2 SPP based Microprocessors

SPP-based photonics is a popular area of nanotechnology and intense research is being done in the area. Some research aims to construct SPP based microprocessors that theoretically can work at frequencies 100.000 greater than the silicon based microchips of today. Electronic components such as wires and transistors have a limited data transfer capacity, but can be fabricated in extremely small sizes. Photonic components such as fibre optic cables have a large data transfer capacity, but are large compared to electronic circuits. By combining the size of electronic components with the capacity of fibre optic cables, microprocessors with superior properties can be fabricated. SPPs could be the solution that combines the two technologies. [Brongersma, 2007]

The potential of fabricating microprocessors utilizing SPPs is mainly limited by the fact that the propagation length of SPPs is only a few tens of micrometers. The size of a chip is greater than that so an SPP will be unable to travel the whole length. The length an SPP can travel before dying out is determined by the dielectric function of the metal it is propagating in, the dielectric constant of the adjacent material and the wavelength of the SPP. The optimal propagation condition is a perfect smooth surface without impurities.

While an all SPP based microchip will require many years of highly focused research in the area, the individual components necessary to build up a chip has been fabricated in the lab. SPP waveguides, mirrors, splitters, and even SPP transistors have been proven possible to fabricate in the lab. By constructing a periodic array of nanoparticles on a metal surface with a lattice constant comparable to the wavelength of the incoming SPP, it is possible to create areas on the surface where no SPP modes are available and propagation through these areas are forbidden. This is in direct analogy to electron propagation in a periodic lattice in a crystal. In this way it is possible to guide the SPP on the surface of a metal. Mirrors can be created in the exact same manner, reflecting the incoming SPP, and by constructing an appropriate array of nanoparticles on the surface SPP beamsplitters can be created.

1.3 Focusing of SPPs

When an SPP beam is excited on a metal surface it is possible to focus the beam in a point with dimensions far below the diffraction limit of optical light. This can be done by introducing a parabolic chain of nanoparticles on the surface. The principle behind the SPP focusing is the same as the principle behind focusing of radio signals for television viewing. If the chain is fabricated in such a way that the SPP incident on the structure impinges the parabola branches at an oblique angle the SPP is reflected and collected in the parabola focal point. As will be described later, these structures also exhibit properties for beam splitting of SPP beams.

1.4 Leakage Radiation Microscopy

Because of the exponentially decaying SPP fields away from the surface it is not possible to use traditional far-field techniques to map the fields from SPPs. Instead, near-field microscopes are used in different ways to investigate e.g. the propagation of SPPs on a surface. One way of doing this is to scan an optical fibre tip above the surface in the same manner as is done in AFM or STM microscopy. The distance from the tip to the surface is crucial for the resolution of the obtained image. This technique is thus very time consuming though. Another technique

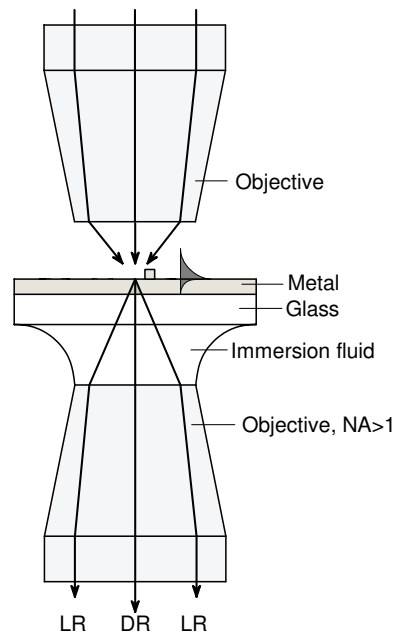


Figure 1.1: Sketch of a leakage radiation microscopy arrangement. The metal surface is radiated from above through an objective, focusing the light at the metal/air interface. A high numerical aperture microscope objective is directly imaging the leakage radiation that emerges from the glass. Between the high numerical aperture objective and the glass an immersion contact is placed to avoid TIR at the glass/air interface and allow light to enter the objective. After the objective the leaked radiation (LR) is recorded by a CCD camera. Modified from [Bouhelier et al., 2001]

capable of mapping the SPP fields is “leakage radiation microscopy”, illustrated on Fig. 1.1. Here a modified metal film is radiated from above through an objective. SPPs are excited at the metal/air interface with fields decaying exponentially through the metal film to the metal/glass interface. At the glass/air interface an immersion fluid is placed with a refractive index close to that of the glass, avoiding TIR and allowing light to enter the objective. The light is now magnified and can be recorded by a CCD camera to create an image of the leaked radiation. A problem occurs though, because not only the leaked radiation (LR) from the SPPs enters the objective but also the direct radiation (DR) from the light source enters. This radiation is removed before it reaches the camera by using a Fourier filter. [Bouhelier et al., 2001]

1.5 Biosensors

In the Kretschmann configuration of SPP excitation the SPPs are excited on a thin film of a material supporting SPPs. This material is often chosen to be gold. The propagation properties of the SPPs depend heavily on the environment of the thin film so that they can be easily changed by modifying the local environment of the film. This heavy dependence on the environment can be used to create a sensor which is sensitive to molecules that adsorb to the surface of the film. Many bio-molecules contain functional groups with sulphur atoms which creates strong bonds to gold thereby enabling detection of such molecules by measuring the excitation angle of SPPs on the gold surface. Bio-molecules which do not contain sulphur

groups natively can be modified to contain sulphur groups on the surface in order to allow detection. This modification can for example be accomplished by means of mercapto-alkane linkers [Petersen et al., 2006].

1.6 Purpose of the Project

The project can be divided into an experimental part and a theoretical part, both dealing with the same subjects, namely excitation and propagation of SPPs on gold films. The primary aim of the project will be to investigate the effect of SPPs interacting with nanostructures on gold films. These interactions will be examined through both experiments and by setting up theoretical models that describe them. By theoretically modelling the experiments, the validity of the models can be discussed. The experiments dealing with SPP propagation will only examine SPPs interacting with parabolic chains of nanoparticles on the surface of a gold film. As written above, it should be possible to focus the SPP in this way. To visualize this propagation, a leakage radiation microscopy setup will be used. The theoretical background for this setup will be treated and the setup in general will be described further. Some preliminary experiments treating excitation of SPPs will be done in order to develop an understanding for the underlying theory. To perform these experiments a setup capable of measuring the intensity of a reflected beam as a function of the incoming angle in the Kretschmann-Raether configuration has to be build.

Chapter 2

Theory

Contents

2.1	Physics of SPPs	13
2.1.1	SPP Dispersion Relation	14
2.1.2	Excitation of SPP	17
2.1.3	Quantitative Description of Minimum Reflected Intensity	19
2.1.4	Attenuated Total Reflection - ATR	20
2.1.5	Spatial Extension and Propagation Length of SPPs	21
2.2	Scalar Model	23
2.3	Single Particle Scattering	25
2.4	Vectorial Model	26
2.4.1	Two Dipole Resonance	28
2.4.2	Near Field of a Dipole	30
2.4.3	Indirect Propagator	31
2.4.4	Relation to Surface Plasmon Polaritons	33
2.4.5	Connection to Scalar Model	34
2.4.6	In Plane Scattering of SPPs	35

This chapter describes the theory behind the fundamental properties of SPPs. This includes a derivation of the dispersion relation of surface plasmons, the theory behind excitation of SPPs and models for describing the scattering of SPPs by nanoparticles.

2.1 Physics of SPPs

When light is used to excite SPPs, it is important to consider the correlation between the wavevector of the light and the wavevector of the SPP. If these do not match, no SPPs will be excited. To investigate this, the SPP dispersion relation will be derived and compared with that of light to understand the physics of SPP excitation.

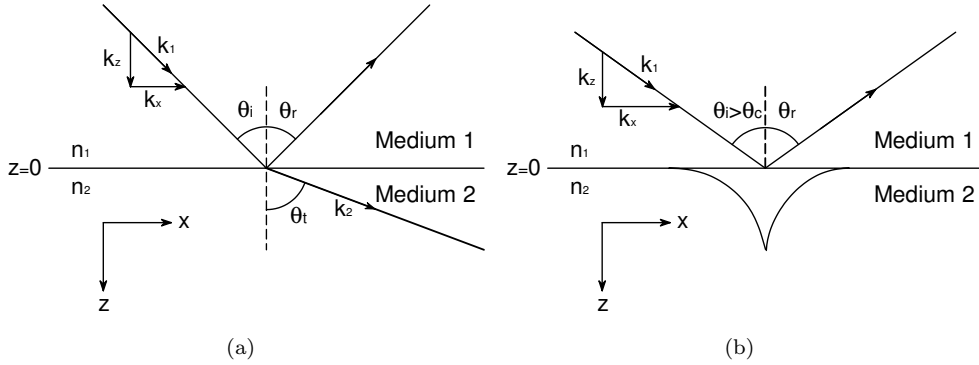


Figure 2.1: (a) Illustration of the incoming, reflected, and transmitted light. The angles θ_i and θ_r are equal. (b) The angle of the incoming light is greater than the critical angle and no light is transmitted. The exponential decay of the evanescent field in medium 2 is illustrated.

2.1.1 SPP Dispersion Relation

In this section the dispersion relation of SPPs on the surface of a semi-infinite solid is derived. Consider p-polarized electromagnetic radiation with wavevector k_1 incident on a planar interface between two media, as seen on Fig. 2.1. The wave is propagating from a medium with high refractive index to a medium with low refractive index. The second medium is a non-magnetic material with relative permeability of unity at the frequency of the incident radiation. As the electric field of the radiation is in the plane of incidence (the plane containing both \mathbf{E} and \mathbf{k}_1) it is described by two components, E_z and E_x in the x - z plane. The magnetic field is tangential to the interface between the two media and is described only by H_y .

The electric and magnetic fields in the two media has to be solutions to the electromagnetic wave equation and are described as

$$z < 0 \quad \mathbf{E}_1 = (E_{x1}, 0, E_{z1}) e^{i(k_{x1}x - \omega t)} e^{ik_{z1}z} \quad (2.1)$$

$$\mathbf{H}_1 = (0, H_{y1}, 0) e^{i(k_{x1}x - \omega t)} e^{ik_{z1}z} \quad (2.2)$$

$$z > 0 \quad \mathbf{E}_2 = (E_{x2}, 0, E_{z2}) e^{i(k_{x2}x - \omega t)} e^{ik_{z2}z} \quad (2.3)$$

$$\mathbf{H}_2 = (0, H_{y2}, 0) e^{i(k_{x2}x - \omega t)} e^{ik_{z2}z}, \quad (2.4)$$

where the wavevectors k_{xi} are given as $k_{xi} = k_{xi}^0 n_i$, and similar with k_{zi} , where k^0 is the free space wavevector and n_i is the refractive index of the medium.

By inserting the expressions for the electric field into the Helmholtz equation, which states that $\nabla^2 \mathbf{E} + \epsilon k^2 \mathbf{E} = 0$, the connection between the x - and z -component of the wavevector and the magnitude of the wavevector in a medium characterized by ϵ is found as

$$k_x^2 + k_z^2 = k^2 \epsilon. \quad (2.5)$$

The tangential components of the fields, E_x and H_y , across the interface between the two media has to be continuous according to the boundary conditions. Therefore

$$E_{1x} = E_{2x} \quad (2.6)$$

$$E_{x1}e^{i(k_{x1}x-\omega t)} = E_{2x}e^{i(k_{x2}x-\omega t)}. \quad (2.7)$$

where E_{1x} and E_{2x} are the x components of the fields in the two media. Since this condition has to be fulfilled for all x values, the tangential components of the wavevector on each side of the interface are equal, $k_{x1} = k_{x2} = k_x$. This leads to the conditions

$$E_{x1} = E_{x2} \quad (2.8)$$

$$H_{y1} = H_{y2}. \quad (2.9)$$

By applying Maxwell's equation $\nabla \cdot \mathbf{E} = 0$ on the electric fields above the relationship between the x and z-component of the amplitude in each medium is found as (for calculation see App. A)

$$E_{z1} = -E_{x1} \frac{k_x}{k_{z1}} \quad (2.10)$$

$$E_{z2} = -E_{x2} \frac{k_x}{k_{z2}}. \quad (2.11)$$

The relationship between the electric field and the magnetic field is described through Faraday's law, which states that $\nabla \times \mathbf{E} = -\mu \frac{d\mathbf{H}}{dt}$. By inserting the fields from Eqn. 2.1 to 2.4 the following relationship is found (for calculation see App. A)

$$H_{y1} = \frac{\omega E_{x1} \varepsilon_1 \varepsilon_0}{k_{z1}} \quad (2.12)$$

$$H_{y2} = \frac{\omega E_{x2} \varepsilon_2 \varepsilon_0}{k_{z2}}. \quad (2.13)$$

By introducing the boundary conditions, Eqn. 2.8 and 2.9, to these equations the relationship between the normal components of the wavevectors in both media is easily obtained as

$$\frac{\varepsilon_1}{k_{z1}} = \frac{\varepsilon_2}{k_{z2}}. \quad (2.14)$$

The wavenumbers k_{z1} and k_{z2} can be expressed through Eqn. 2.5 as

$$k_z = (\varepsilon k^2 - k_x^2)^{1/2}. \quad (2.15)$$

For the fields in Eqn. 2.1 to Eqn. 2.4 to be surface waves, it is required that k_z is purely imaginary. This is satisfied when $k_x^2 > \varepsilon k^2$, which yields

$$k_z = \pm i (k_x^2 - \varepsilon k^2)^{1/2}, \quad (2.16)$$

where \pm is included to avoid exponential increasing non physical fields. When this requirement to the wavevectors is fulfilled the obtained wave from Eqn. 2.1 to 2.4 is a trapped surface wave, or evanescent wave, with exponential decay into both media. From the requirement that $k_x^2 > \varepsilon_1 k^2$ it is clear that in the dielectric characterized by ε_1 the wavevector k_x is greater than the maximum wavevector, $\sqrt{\varepsilon_1}k$, available in the dielectric. When comparing k_z from Eqn. 2.16 when $z > 0$ with k_z when $z < 0$ it is obvious that ε_1 and ε_2 from Eqn. 2.14 are of opposite sign since the k_z 's are of opposite sign. If k_{z1} and k_{z2} obtained from Eqn. 2.16 are substituted into Eqn. 2.14 the following equation is obtained for k_x

$$k_x = k \left(\frac{\varepsilon_1 \varepsilon_2}{\varepsilon_1 + \varepsilon_2} \right)^{1/2}. \quad (2.17)$$

Notice that for a propagating mode k_x has to be real which requires $|\varepsilon_2| > \varepsilon_1$ when taking ε_2 as negative, so that the fraction becomes positive. In real metals the oscillations created by an incident electric field is damped due to absorption and an imaginary part is added to the permittivity $\varepsilon_2 = \varepsilon_{2r} + i\varepsilon_{2i}$. By inserting this into Eqn. 2.17 an imaginary part is added to the wavenumber which becomes $k_x = k_{xr} + ik_{xi}$. The real and the imaginary part of k_x is given by [Raether, 1986]

$$k_{xr} = \frac{\omega}{c} \left(\frac{\varepsilon_1 \varepsilon_{2r}}{\varepsilon_1 + \varepsilon_{2r}} \right)^{1/2} \quad (2.18)$$

$$k_{xi} = \frac{\omega}{c} \left(\frac{\varepsilon_1 \varepsilon_{2r}}{\varepsilon_1 + \varepsilon_{2r}} \right)^{3/2} \frac{\varepsilon_{2i}}{2\varepsilon_{2r}^2} \quad (2.19)$$

Eqn. 2.17 is the surface plasmon dispersion relation, which can be seen by inserting $k = \omega/c$, yielding

$$\omega(k_x) = ck_x \left(\frac{\varepsilon_1 \varepsilon_2}{\varepsilon_1 + \varepsilon_2} \right)^{-1/2}. \quad (2.20)$$

The SPP dispersion relation is plotted in Fig. 2.2(a) together with the dispersion relation of EM radiation in vacuum, $\omega = ck_x$. In the plot, the permittivity of the metal, ε_2 of Eqn. 2.20 is inserted as $\varepsilon_2 = 1 - \omega_p^2/(\omega(\omega + i\Gamma))$ where the damping Γ is set to zero. This is the nonretarded electrostatic approximation for the dielectric function. In the limit where $k \rightarrow \infty$, the SPP dispersion relation runs asymptotically against the “cut-off” frequency $\omega_{\text{cut}} = \omega_p/\sqrt{1 + \varepsilon_1}$ as seen on Fig. 2.2(a) where the dotted line indicates ω_{cut} . This is the highest frequency at which an SPP state exists. As can be seen from Fig. 2.2(a), at frequencies over ω_{cut} , there are no allowed states for SPPs, so that EM radiation at these frequencies cannot excite SPPs. At frequencies below ω_{cut} the EM radiation has a smaller wavenumber, k_x , than SPPs. EM radiation at these frequencies therefore has smaller momentum, $\hbar k$, than required to excite SPPs. This problem will be treated further below. At large k_x the SPP group velocity goes to zero as seen on Fig. 2.2(b). In this case the SPPs become a localized fluctuation of the charge distribution and no energy will propagate in the system.

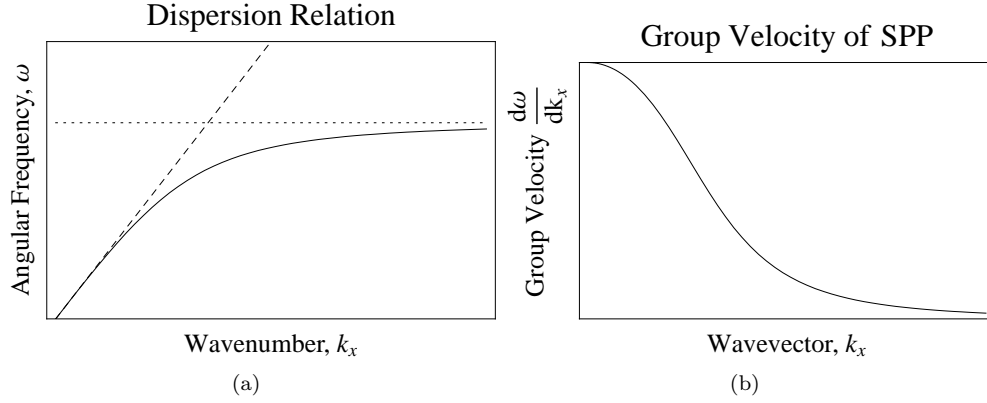


Figure 2.2: (a) Plot of the SPP dispersion relation (solid line) and the dispersion relation of EM radiation in vacuum (dashed line). The dotted line indicates the “cut-off” frequency, ω_{cut} , of the SPP dispersion relation. Both the angular frequency, ω , and the wavenumber, k , is in arbitrary units. (b) x -component of the group velocity of an SPP.

2.1.2 Excitation of SPP

When light impinges an interface at an angle θ between two media it is partially reflected and partially transmitted as illustrated in Fig. 2.1(a). The angle of reflection is equal to the angle of incoming light, while the angle of the transmitted part of the light is determined by Snell’s law which states that $n_1 \sin \theta_i = n_2 \sin \theta_t$. The angle of the incoming light at which the angle of the transmitted light equals $\pi/2$ is called the critical angle, given by $\theta_c = \arcsin n_2/n_1$. When θ_i exceeds the critical angle, all the light is reflected and no light is travelling inside medium 2. If the refractive index of medium 1 is higher than that of medium 2 the light has suffered total internal reflection. Even though all the light is reflected back into medium 1, an exponentially decaying field, an evanescent field, still exists in medium 2 as illustrated in Fig. 2.1(b).

When using light to excite SPPs a difficulty is met since the SPP dispersion relation lies to the right of the light line i.e. $k_{\text{SPP},x} > \omega/c$, as seen on Fig. 2.2(a). If light at a given frequency ω is used the momentum $\hbar\omega/c$ has to be increased by an amount Δk_x in order to transform the light into SPPs. A way to accomplish this is to guide EM radiation through a prism placed above the surface of a metal film. Utilizing this technique, different geometries can be used. In the Otto geometry the prism is placed above the metal film with an air gap between the film and the prism less than a few wavelengths thick [Raether, 1986] [Sambles et al., 1991]. This provides an evanescent tunnel barrier with which the radiation couples and an SPP is exited at the metal/air interface. Another geometry is the Kretschmann-Raether geometry [Raether, 1986] [Sambles et al., 1991]. Here the metal film is coated onto the prism so no air gap is present. When the angle of incidence is greater than the critical angle, $\theta_i > \theta_c$, total internal reflection is achieved and $k_x^2 > k^2 \epsilon$. An evanescent wave is propagating along the interface with its field amplitude decreasing exponentially into the metal film, see Fig. 2.1(b). The transmitted wave takes the form as in Eqn. 2.1

$$E_t(x, z, t) = e^{ik_z z} e^{i(\omega t - k_{ix} x)}, \quad (2.21)$$

where $k_{ix} = k_i \sin(\theta_i)$, the x -component of the wavevector of the incoming EM radiation and k_z is given by Eqn. 2.16. By considering the propagating term of Eqn. 2.21 it is obtained that as

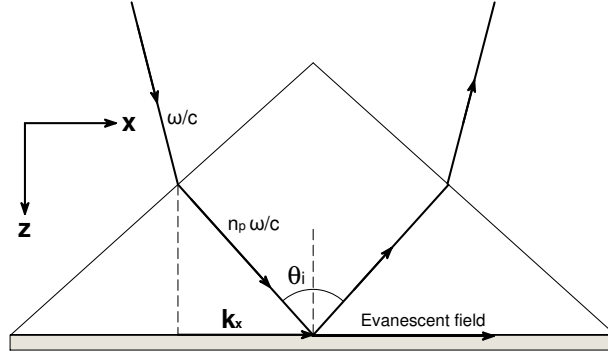


Figure 2.3: Kretschmann-Raether geometry of the prism and the metal film. The evanescent field is indicated at the prism/metal interface. The projection of incoming light through a dielectric medium on the metal film yields $k_x = \omega/c\sqrt{\epsilon_p} \sin \theta$ while the projection of light through air yields $k_x = \omega/c \sin \theta$.

the angle of the incoming EM radiation is varied, k_{ix} changes and the phase of the evanescent wave changes. When a k_{ix} is chosen that satisfies the SPP dispersion relation at a given ω resonance occurs and an SPP can be excited. At this angle of incidence of the incoming EM radiation, the momentum of the radiation is equal to the momentum of the SPP.

In Fig. 2.2(a) the dispersion relation for SPPs on a semi-infinite solid is plotted. At all k_x the SPP dispersion is to the right of the light line in vacuum, i.e. light cannot be converted into SPPs because of the missing momentum $\hbar \Delta k_x$. When using the Kretschmann-Raether geometry, light is reflected at a metal surface covered with a dielectric medium, e.g. quartz. When light is travelling inside the dielectric medium its momentum is different from that of light travelling in vacuum (air). The momentum of light inside quartz is $\hbar \sqrt{\epsilon_p} \omega/c$, which is different from that of vacuum $\hbar \omega/c$. k_x is therefore different when light impinges the metal through a dielectric medium than if it impinges the metal through air, see Fig. 2.3. The dispersion relation of a medium characterized by ϵ is expressed through Eqn. 2.5 as $k_z^2 = k^2 \epsilon \cos^2 \theta$ yielding

$$\begin{aligned} k_x^2 &= k^2 \epsilon - k^2 \epsilon \cos^2 \theta \\ k_x^2 &= k^2 \epsilon \sin^2 \theta \\ k_x &= \sqrt{\epsilon} \frac{\omega}{c} \sin \theta \quad \Rightarrow \quad \omega = k_x \frac{c}{\sqrt{\epsilon} \sin \theta} \end{aligned} \quad (2.22)$$

where θ is the angle at which SPPs are excited. The dispersions for a prism and for air are plotted on Fig. 2.4, where the blue line is the dispersion relation Eqn. 2.20, line (1) is the dispersion of the projection on the x-axis of light in vacuum, line (2) is the dispersion of light in vacuum, line (3) is the dispersion of the projection on the x-axis of light in a medium ϵ , line (4) is the dispersion of light in a medium ϵ . Notice that the dispersion of light in air is located left of the SPP dispersion relation for all k_x , i.e. no SPPs can be excited. Since the dispersion of light through a dielectric medium lies at the right side of the SPP dispersion relation up to a certain k_x , light can excite SPPs of frequencies below this point at the metal/air interface.

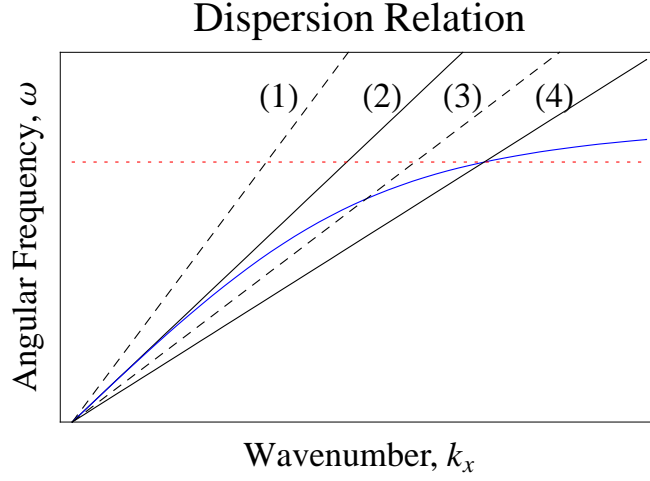


Figure 2.4: Dispersion relation of SPPs for a quartz/metal/air system. Eqn. 2.20 is compared to the dispersion of light in air and in quartz and the projections on the x -axis of light in air and in quartz. The black lines represent the dispersion of light in vacuum and the projection on the x -axis. The dashed lines are the dispersion of light in quartz and the projection on the x -axis. The dispersion of light in quartz intersects the SPP dispersion at the point marked by the red dotted line.

2.1.3 Quantitative Description of Minimum Reflected Intensity

The resonance situation described above can be calculated for a given system by Fresnel reflection theory for a two interface system. The total reflectivity is calculated in appendix B and is given by

$$R(\theta) = \left| \frac{E_r}{E_{in}} \right|^2 = \left| \frac{r_{pm} + r_{ma} e^{2ik_{zm}d}}{1 + r_{pm}r_{ma} e^{2ik_{zm}d}} \right|^2, \quad (2.23)$$

where r_{pm} and r_{ma} is the single interface reflection coefficient of the prism/metal and the metal/air interface respectively. These are given by

$$r_{pm} = \frac{\frac{k_{zp}}{\varepsilon_p} - \frac{k_{zm}}{\varepsilon_m}}{\frac{k_{zp}}{\varepsilon_p} + \frac{k_{zm}}{\varepsilon_m}}, \quad (2.24)$$

$$r_{ma} = \frac{\frac{k_{zm}}{\varepsilon_m} - \frac{k_{za}}{\varepsilon_a}}{\frac{k_{zm}}{\varepsilon_m} + \frac{k_{za}}{\varepsilon_a}}, \quad (2.25)$$

where k_{zp} , k_{zm} and k_{za} are expressed through Eqn. 2.5

$$k_x^2 + k_{zi}^2 = \varepsilon_i \left(\frac{\omega}{c} \right)^2. \quad (2.26)$$

Here k_x is the x component of the wavevector of the incoming EM radiation in the prism and k_{zi} is the z component of the EM radiation in medium i . k_x can be written as $k_x = k \sin \theta$

where k is the wavevector of the EM radiation in the prism given by $k = 2\pi n_p/\lambda$. k_{zi} can be written as

$$\begin{aligned} \left(\frac{2\pi n_p}{\lambda} \sin \theta\right)^2 + k_{zi}^2 &= \varepsilon_i \left(\frac{2\pi}{\lambda}\right)^2 \\ k_{zi} &= \left[\varepsilon_i \left(\frac{2\pi}{\lambda}\right)^2 - \left(\frac{2\pi n_p}{\lambda}\right)^2 \sin^2 \theta \right]^{1/2} \\ k_{zi} &= \frac{2\pi}{\lambda} [\varepsilon_i - \varepsilon_p \sin^2 \theta]^{1/2}. \end{aligned} \quad (2.27)$$

2.1.4 Attenuated Total Reflection - ATR

To investigate the excitation of SPPs a phenomenon known as attenuated total reflection is utilized. A setup for SPP excitation using ATR is the Kretschmann configuration discussed earlier. When light impinges the prism/metal interface it is partially reflected and partially transmitted into the metal as an exponentially decaying fields. At the metal/air interface the field excites SPPs which radiates light back. In the prism this radiated light interfere destructively with the reflected light since the two waves are in anti phase. If the thickness of the metal film is increased, the internal damping is increased and the degree of SPP excitation is decreased. The radiated field disappears and no destructive interference takes place. The reflection coefficient, R , then approaches unity. If the thickness of the film is decreased the radiated field is increased and R is reduced. When the metal film has an ideal thickness, d_i , the reflected field and the radiated field cancel out and R becomes zero. Because of energy conservation the sum of the relative reflected, transmitted, and absorbed part of the light energy equals unity, $R + T + A = 1$. Since $T = 0$ and at $d = d_i$, $R = 0$ then $A = 1$, i.e. all the light energy is absorbed in the metal film.

The dispersion relation derived in Sec. 2.1.1 was calculated for a semi-infinite metal. This is not the case for the Kretschmann configuration where the metal layer is of finite thickness. When the thickness of the metal layer decreases, the medium ε_p e.g. quartz approaches the interface metal/air and influences the wavevector k_x by adding an additional term Δk_x , so that the new resonance position becomes $k_x = k_x^0 + \Delta k_x$. Here k_x^0 is the wavevector of the dispersion relation from Eqn. 2.20. The internal damping in the metal is given by $\Gamma_i = \text{Im}\{k_x^0\}$. When adding the term Δk_x an additional damping is added which is $\Gamma_{\text{rad}} = \text{Im}\{\Delta k_x\}$. This damping term is due to the radiation caused by SPPs on the metal/air interface that escapes the metal film and radiates back into the dielectric medium in the direction of the reflected light. The total damping in the metal film now becomes

$$\Gamma_{\text{total}} = \text{Im}\{k_x^0\} + \text{Im}\{\Delta k_x\} \quad (2.28)$$

$$\Gamma_{\text{total}} = \Gamma_i + \Gamma_{\text{rad}}. \quad (2.29)$$

In the case of total internal reflection at the quartz/metal interface, an expression for the reflectivity of the dielectric/metal/air system in terms of the damping is derived by [Raether, 1986] yielding

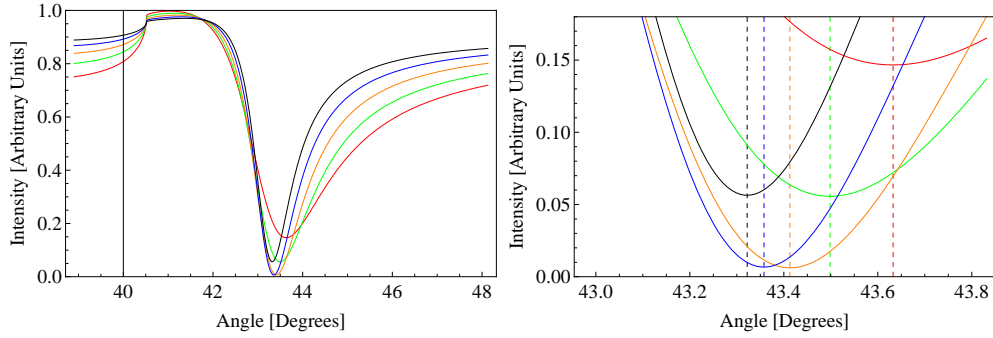


Figure 2.5: Plot of the reflectivity curve of the three layer system prism/metal/air at two different zoom levels. The thickness of the metal layer is varied on the five plotted curves, the red curve shows the reflectivity with a metal thickness of 40nm, the green curve 45nm, the orange curve 50nm, the blue curve 55nm and the black curve 60nm. Notice that both the height and angle of the minimum of reflection changes when the thickness is varied. The following parameters are used: $\epsilon_p = 2.4$, $\epsilon_m = -9.89 + i1.05$ [Palik, Empty], $\epsilon_a = 1$, $\lambda = 632.8\text{nm}$.

$$R = 1 - \frac{4\Gamma_i\Gamma_{\text{rad}}}{[k_x - (k_x^0 + \Delta k_x)]^2 + (\Gamma_i + \Gamma_{\text{rad}})^2}. \quad (2.30)$$

In the resonance situation $k_x = k_x^0 + \Delta k_x$, Eqn. 2.30 reduces to

$$R = 1 - \frac{4\Gamma_i\Gamma_{\text{rad}}}{(\Gamma_i + \Gamma_{\text{rad}})^2}. \quad (2.31)$$

It is now obvious that R passes a minimum which is zero when $\Gamma_i = \Gamma_{\text{rad}}$, i.e. when the internal damping in the metal is equal to the damping due to radiation caused by SPPs in the metal/air interface, R becomes zero and all the light energy is absorbed in the metal. This is the optimal condition for excitation of SPPs.

Fig. 2.5 demonstrates the effect of varying the thickness of the metal layer on the resonance angle and its height, while other parameters are held constant. Notice that as the thickness of the metal layer is increased the minimum of the function changes. It is possible to obtain an ideal thickness at which the reflectivity equals zero, see Fig. 2.6. Notice that when the thickness of the metal layer is increased, the position of minimum reflection is displaced toward a smaller angle. As the thickness is changed, Γ_{rad} changes while Γ_i remains constant, it is therefore possible to put $\Gamma_{\text{rad}} = \Gamma_i$ and obtain an ideal thickness of the metal layer.

2.1.5 Spatial Extension and Propagation Length of SPPs

As described above the SPP field amplitude decreases exponentially normal to the surface as $\exp(-|k_{zi}z|)$. The depth at which the field falls to $1/e$ is expressed as

$$z_d = \frac{1}{|k_{zi}|}, \quad (2.32)$$

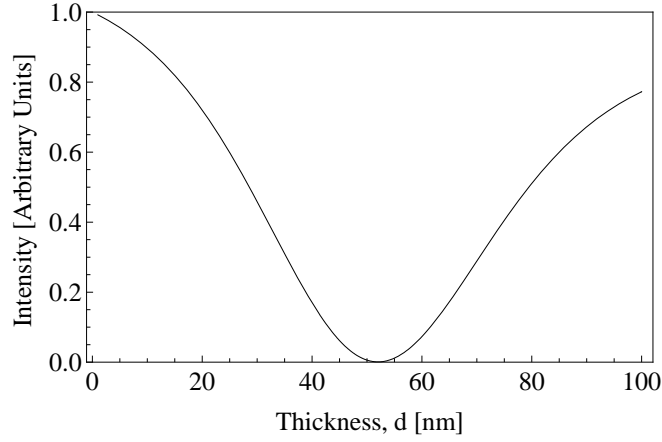


Figure 2.6: Plot of reflectivity as a function of metal thickness. The ideal metal thickness is in this case 51nm. The following parameters are used in the calculation: $\theta = 0.7576$ rad, $\varepsilon_m = -9.89 + i1.05$, $\varepsilon_p = 2.4$, $\lambda = 632.8$ nm

where k_{zi} is the z-component of the wavevector in the material of interest, given as

$$k_{zi} = \left[\varepsilon_i \left(\frac{\omega}{c} \right)^2 - k_x^2 \right]^{1/2}, \quad (2.33)$$

and k_x given by Eqn. 2.17. By inserting k_x in Eqn. 2.33, the z-component of the wavevector in the metal yields

$$\begin{aligned} k_{zm} &= \left[\varepsilon_m \left(\frac{\omega}{c} \right)^2 - \left(\frac{\omega}{c} \right)^2 \frac{\varepsilon_a \varepsilon_m}{\varepsilon_a + \varepsilon_m} \right]^{1/2} \\ &= \frac{\omega}{c} \left[\varepsilon_m - \frac{\varepsilon_a \varepsilon_m}{\varepsilon_a + \varepsilon_m} \right]^{1/2} \\ &= \frac{2\pi}{\lambda} \left[\frac{\varepsilon_m(\varepsilon_a + \varepsilon_m) - \varepsilon_a \varepsilon_m}{\varepsilon_a + \varepsilon_m} \right]^{1/2} = \frac{2\pi}{\lambda} \left[\frac{\varepsilon_m^2}{\varepsilon_a + \varepsilon_m} \right]^{1/2}, \end{aligned} \quad (2.34)$$

where ε_m is the real part of the permittivity of the metal, ε is the permittivity of air, and λ is the free space wavelength of the incoming EM radiation. The expression for the SPP depth in the metal becomes

$$z_{dm} = \frac{\lambda}{2\pi} \left[\frac{\varepsilon_a + \varepsilon_m}{\varepsilon_m^2} \right]^{1/2}, \quad (2.35)$$

and likewise the SPP depth in the air becomes

$$z_{da} = \frac{\lambda}{2\pi} \left[\frac{\varepsilon_a + \varepsilon_m}{\varepsilon_a^2} \right]^{1/2}. \quad (2.36)$$

For $\lambda = 650$ nm, the permittivity of gold and silver are -12.9 and -19 respectively [Raether, 1986]. This yields for gold $z_{\text{dm}} = 25.5$ nm and $z_{\text{da}} = 329.4$ nm and for silver $z_{\text{dm}} = 21.3$ nm and $z_{\text{da}} = 405.1$ nm.

Once light has been converted into a propagating SPP on a flat metal surface it will gradually attenuate because of losses due to absorption in the metal. This attenuation depends on the dielectric function of the metal at the SPP wavelength. As the SPP propagates along the surface of the metal the intensity decreases as $\exp(-2k_{xi}x)$ with k_{xi} given by Eqn. 2.19. The length travelled after which the intensity has decreased to $1/e$ is given by

$$\delta_{SPP} = \frac{1}{2k_{xi}} = \frac{\lambda}{2\pi} \left(\frac{\varepsilon_{mr} + \varepsilon_p}{\varepsilon_{mr}\varepsilon_p} \right)^{3/2} \frac{\varepsilon_{mr}^2}{\varepsilon_{mi}}, \quad (2.37)$$

where λ is the free space wavelength and ε_{mr} and ε_{mi} is the real and imaginary part of the permittivity of the metal respectively. Silver is the metal with the lowest losses in the visible spectrum [Barnes et al., 2003], yielding propagation lengths of around $10\mu m$. By using light of a longer wavelength the propagation length increases. The SPP propagation length determines the upper limit of the size of any photonic circuit based on SPPs.

2.2 Scalar Model

When an SPP propagating on the surface of a metal hits an irregularity the SPP is scattered in all directions. This model is a simple description of SPP scattering by nanoparticles on a surface [Bozhevolnyi and Coello, 1998]. The model is based on three main assumptions:

1. Elastic (in the plane) scattering of SPPs dominates over inelastic (out of the plane) scattering.
2. The scattered SPP field is an isotropic cylindrical wave propagating outwards from the scatterer.
3. The z-component of the field is much larger than the x and y component.

The incident SPP field is described by a plane wave. In Fig. 2.7(a) scattering by a single nanoparticle is shown. It can be seen that the wavefronts of the scattered waves are isotropic and cylindrical. When more than one scatterer is present all the scattered waves and the incident field interfere. The field at any arbitrary point due to this interference can be calculated by the expression

$$E(\mathbf{r}) = E_0(\mathbf{r}) + \sum_{i=1}^N \alpha_i E(\mathbf{r}_i) G(\mathbf{r}, \mathbf{r}_i). \quad (2.38)$$

In this expression α_i is the polarizability of the i 'th scatterer and G is the field propagator. The field propagator describes how the field propagates on the surface and how it is scattered. In this model the propagator is simply given by

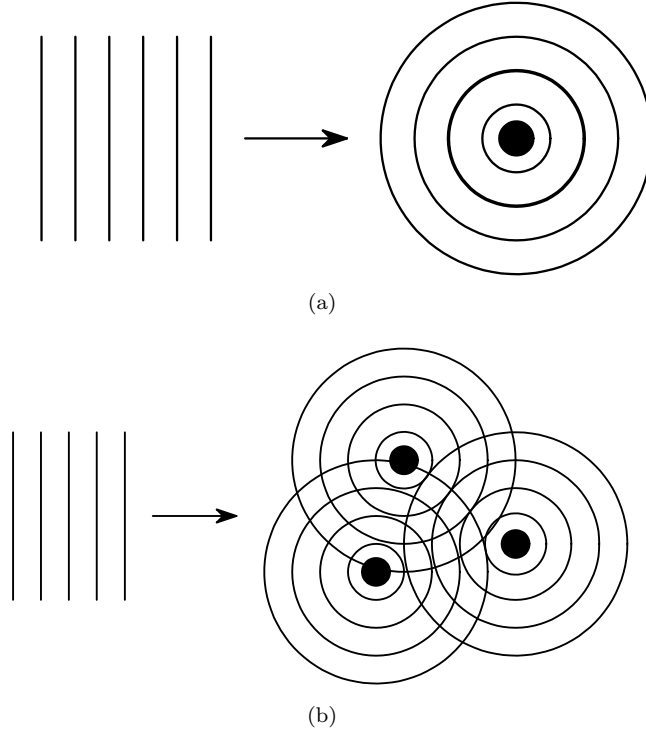


Figure 2.7: (a) Scattering of a plane SPP (b) Interference between scattered SPPs

$$G(\mathbf{r}, \mathbf{r}_i) = \frac{i}{4} H_0^{(1)}(k_{\text{SPP}} |\mathbf{r} - \mathbf{r}_i|), \quad (2.39)$$

where $H_0^{(1)}$ is the 0'th order Hankel function of first kind and k_{SPP} is the propagation constant of SPPs (Sec. 2.1). From this expression and Eqn. 2.38 it can be seen that the scattered field propagates as a cylindrical wave 90° out of phase with the incoming field. The Hankel function ensures the correct behaviour of the scattered wave, i.e. the scattered field intensity decreases as $1/x$. The phase difference reflects the fact the particle does not respond immediately to the incoming radiation, there is some delay. Also, if there was no phase difference there would be constructive interference between the incoming and scattered radiation and this would not conserve energy.

Before the expression Eqn. 2.38 can be of any use though, the fields at the sites of the scatterers, $E(\mathbf{r}_i)$, has to be known. These fields can be calculated from

$$E(\mathbf{r}_i) = E_0(\mathbf{r}_i) + \sum_{j=1, j \neq i}^N \alpha_j E(\mathbf{r}_j) G(\mathbf{r}_i, \mathbf{r}_j). \quad (2.40)$$

This is a matrix equation which can be easily solved. Thereby the fields at the sites of the scatters are obtained and Eqn. 2.39 can be used to calculate the field at any point on the surface. The incoming SPP field is described by a plane gaussian beam of the form

$$E_0(\mathbf{r}) = e^{-y^2/w^2} e^{i(k_{\text{SPP}}x - \omega t)}, \quad (2.41)$$

where w is the beam waist, y is the distance from the waist of the beam and k_{SPP} is the SPP propagation constant. When the beam waist approaches infinity the wave becomes a plane wave of infinite extent in the direction perpendicular to the direction of propagation.

The polarizability α of the scatterers is determined experimentally, in the sense that the polarizability is simply adjusted until the theoretically predicted results looks similar to the experimental ones. From [Bozhevolnyi and Coello, 1998] the polarizability is approximately $\alpha = 3$. Later in Sec. 2.4.5 an analytical expression for the polarizability will be derived.

2.3 Single Particle Scattering

Single particle scattering is considered analytically in this section in order to illustrate some properties of scattering of surface plasmons.

The starting point is Eqn. 2.38. In the case of only one scatterer this equation reduces to $E(\mathbf{r}) = E_0(\mathbf{r}) + \alpha E(\mathbf{r}_1)G(\mathbf{r}, \mathbf{r}_1)$. Using Eqn. 2.40 it is seen that the field at the scatterer is given simply by $E(\mathbf{r}_1) = E_0(\mathbf{r}_1)$. Therefore, using the expression Eqn. 2.41 with an infinite beam waist for the incident field (the time dependence of the field is ignored, it would cancel out anyway when calculating the intensity) and the expression Eqn. 2.39 for the field propagator, the field at an arbitrary position is given by

$$\begin{aligned} E(\mathbf{r}) &= E_0(\mathbf{r}) + \alpha E_0(\mathbf{r}_1)G(\mathbf{r}, \mathbf{r}_1) \\ &= e^{ik_{\text{SPP}}x} + \alpha e^{ik_{\text{SPP}}x_1} \frac{i}{4} H_0^{(1)}(k_{\text{SPP}} |\mathbf{r} - \mathbf{r}_1|). \end{aligned} \quad (2.42)$$

In the far field limit the Hankel function can be approximated by

$$H_0^{(1)}(x) \approx \sqrt{\frac{2}{\pi}} e^{-i\pi/4} \frac{e^{ix}}{\sqrt{x}}. \quad (2.43)$$

Using this approximation the field is then given by

$$\begin{aligned} E(\mathbf{r}) &= e^{ik_{\text{SPP}}x} + \sqrt{\frac{\alpha^2}{8\pi}} e^{ik_{\text{SPP}}x_1} e^{i\pi/2} e^{-i\pi/4} \frac{e^{ik_{\text{SPP}}|\mathbf{r} - \mathbf{r}_1|}}{\sqrt{k_{\text{SPP}} |\mathbf{r} - \mathbf{r}_1|}} \\ &= e^{ik_{\text{SPP}}x} + \sqrt{\frac{\alpha^2}{8\pi}} \frac{e^{i(k_{\text{SPP}}x_1 + k_{\text{SPP}}|\mathbf{r} - \mathbf{r}_1| + \pi/4)}}{\sqrt{k_{\text{SPP}} |\mathbf{r} - \mathbf{r}_1|}}. \end{aligned} \quad (2.44)$$

The intensity is now calculated assuming that k_{SPP} is a purely real number corresponding to no damping of the propagating field. Since the damping does not matter for the purposes of this analytical treatment, this is not a limitation

$$I(\mathbf{r}) = |E(\mathbf{r})|^2 = 1 + C^2 + 2C \cos(k_{\text{SPP}}x_1 + k_{\text{SPP}}|\mathbf{r} - \mathbf{r}_1| - k_{\text{SPP}}x + \pi/4), \quad (2.45)$$

where $C^2 = \alpha^2/8\pi k_{\text{SPP}} |\mathbf{r} - \mathbf{r}_1|$. If the scatterer is placed at the origin $x_1 = y_1 = 0$ and $|\mathbf{r} - \mathbf{r}_1| = |\mathbf{r}|$, and the above expression simplifies to $I(\mathbf{r}) = 1 + C^2 + 2C \cos(k_{\text{SPP}} |\mathbf{r}| - k_{\text{SPP}} x + \pi/4)$. The argument to the cosine will never be zero because x is at most equal to $|\mathbf{r}|$ in which case the argument will be $\pi/4$. The minimum value of the cosine is thus $1/\sqrt{2}$. The condition for maximum intensity is

$$\sqrt{x^2 + y^2} - x = \lambda_{\text{SPP}} \left(n - \frac{1}{8} \right), \quad (2.46)$$

where $k_{\text{SPP}} = 2\pi/\lambda_{\text{SPP}}$ was used. To see the shape of the fringes of maximum intensity x is expressed as a function of y in the above equation. This can be done quite easily by first moving x to the right side and squaring both sides yielding

$$x^2 + y^2 = \lambda_{\text{SPP}}^2 \left(n - \frac{1}{8} \right)^2 + x^2 + 2\lambda_{\text{SPP}} \left(n - \frac{1}{8} \right) x. \quad (2.47)$$

Cancelling x^2 on both sides the expression $x(y)$ becomes

$$x(y) = \frac{y^2 - \lambda_{\text{SPP}}^2 \left(n - \frac{1}{8} \right)^2}{2\lambda_{\text{SPP}} \left(n - \frac{1}{8} \right)}. \quad (2.48)$$

From this expression it is seen that the fringes have parabolic shapes and that, at $y = 0$, they are separated by a distance of $\lambda_{\text{SPP}}/2$. When n increases the parabola apex moves further down the negative x-axis and the parabola becomes wider. This is illustrated in Fig. 2.8(c). In this picture the scatterer is placed in the origin and the field is approaching the scatterer from the negative x-axis. The parabola shaped fringes are due to interference between the scattered cylindrical wave and the incoming plane wave.

In between the fringes the intensity is not zero. This can be seen from Fig. 2.8(a) where the field intensity along the x-axis ($y = 0$) is plotted. Here it can be seen that on the negative x side of the scatterer the field is oscillating but that behind the scatterer the field is decreasing exponentially.

In Fig. 2.8(b) the intensity is plotted along with the argument to the cosine. The intensity is calculated at points lying on a circle of radius $r = 2.1\mu\text{m}$ centered at the scatterer. The y-scale is given in units of 2π . Using the grid in the figure it can be seen that intensity maxima occurs when the argument to the cosine equals an integral multiple of 2π .

2.4 Vectorial Model

In the scalar model presented in the previous section the vector nature of EM radiation was suppressed and it was assumed that the scattering of an EM wave from a metal nanoparticle could be described by an outgoing isotropic cylindrical wave. In general this will not be the case since the scattering need not be the same in all directions.

In this model the propagator G , which was simply described by a zeroth order Hankel function of the first kind in the scalar model, is described by a tensor which accounts for the fact that the

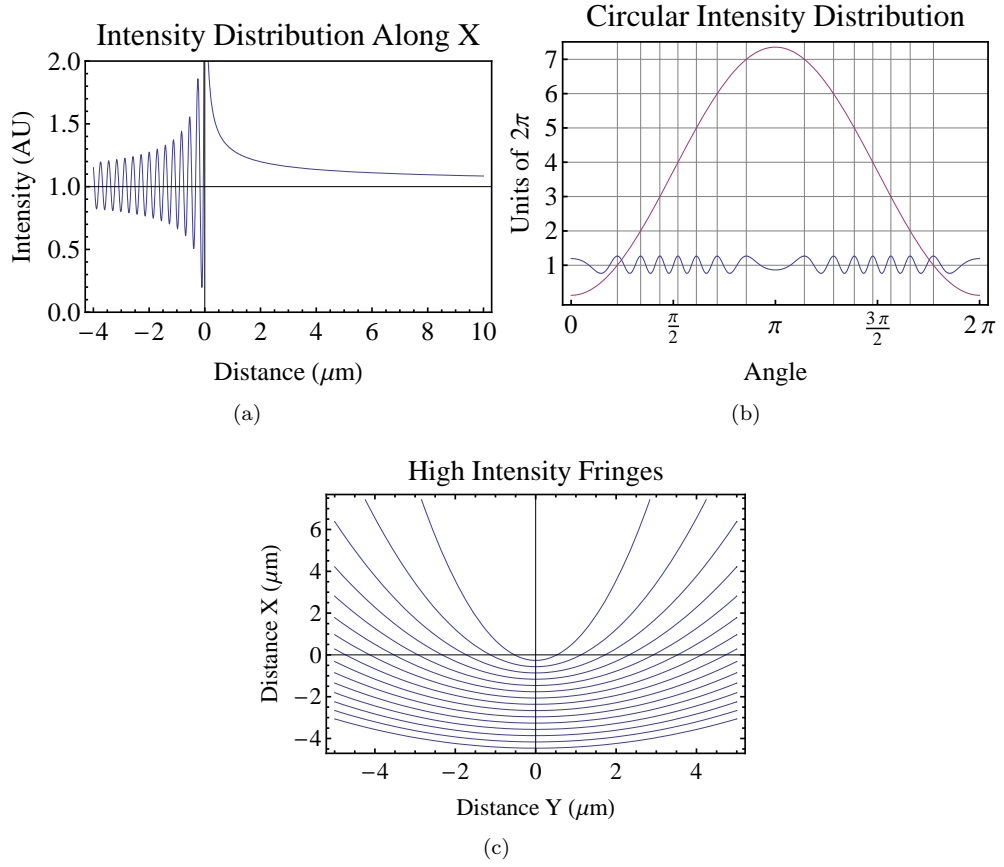


Figure 2.8: (a) Intensity distribution for the scattered field when looking along the x -axis. (b) Intensity distribution when looking in a circle around the scatterer. (c) Fringes of high intensity plotted for $n = 1$ to $n = 15$. The scatterer is located at the origin. It is seen that the fringes have parabolic shapes.

scattered wave doesn't have to be isotropic. Since the incident field will polarize the scatterers (metallic nanospheres) they are described as point dipoles. The propagator is described by two parts, a direct part and an indirect part. This splitting into two parts is done in order to account both for the scattering from a dipole propagating directly to the observation point and the scattering first reflecting off the surface and then propagating to the observation point. This scenario is illustrated in Fig. 2.9. The full propagator is thus given by the expression

$$\hat{G} = \hat{D} + \hat{I}, \quad (2.49)$$

where \hat{D} is the direct propagator and \hat{I} is the indirect propagator. The indirect propagator takes into account propagation of s and p polarized waves from the source to the destination and also propagation by means of SPPs. Later in Sec. 2.4.4 the indirect propagator will be split into its s,p-polarized and SPP components.

The direct propagator is given by the following expression [Keller et al., 1992]

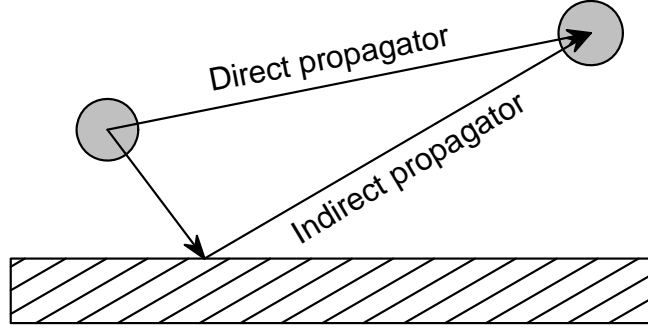


Figure 2.9: The concept of direct and indirect propagation. EM radiation scattered at one dipole propagates to another dipole by both direct and indirect paths, where the indirect path involves reflection in the surface.

$$\hat{\mathbf{D}}(\mathbf{r}, \mathbf{r}') = \frac{1}{4\pi} \left[\left(-\frac{1}{R} - \frac{ic}{\omega R^2} + \frac{c^2}{\omega^2 R^3} \right) \hat{\mathbf{U}} + \left(\frac{1}{R} + \frac{3ic}{\omega R^2} - \frac{3c^2}{\omega^2 R^3} \right) \mathbf{e}_R \mathbf{e}_R \right] e^{i\omega R/c}, \quad (2.50)$$

where \mathbf{r} is the observation point, \mathbf{r}' is the scatterer point, $R = |\mathbf{r} - \mathbf{r}'|$ and $\mathbf{e}_R = (\mathbf{r} - \mathbf{r}')/R$ is a unit vector directed from the scatterer to the observation point. The indirect propagator is more complicated and will be dealt with later in Sec. 2.4.3.

From the form of the direct propagator it can be seen that the propagator approaches a spherical wave at large distances (far field region, $R \rightarrow \infty$). At large distances the only term in the sharp paranthese that survives is the $-1/R$ term.

What is more interesting is the field in the near field region. The near field region is where the distance from the dipole is very small compared to the wavelength. This means that $2\pi R/\lambda = kR \approx 0$, so that only the $1/R^3$ terms survives. In this limit the form of the direct propagator becomes

$$\hat{\mathbf{D}}_{\text{nf}}(\mathbf{r}, \mathbf{r}') = -\frac{c^2}{4\pi\omega^2} \frac{3\mathbf{e}_R \mathbf{e}_R - \hat{\mathbf{U}}}{R^3}. \quad (2.51)$$

In the following section only the near field direct propagation part is considered in order to calculate the resonance condition for two dipoles.

2.4.1 Two Dipole Resonance

When two dipoles are placed near each other so that the distance R between them obeys $kR \approx 0$ a resonance may occur and the field at the sites of the dipoles may become very strong. To calculate the field at the site of the dipole an approach similar to the one used in the scalar model is used. The self consistent field is given by the equation [Keller et al., 1992]

$$\mathbf{E}(\mathbf{r}, \omega) = \mathbf{E}_0(\mathbf{r}, \omega) - \mu_0 \omega^2 \sum_{i=1}^N \alpha_i(\omega) \hat{\mathbf{G}}(\mathbf{r}, \mathbf{r}_i) \mathbf{E}(\mathbf{r}_i, \omega), \quad (2.52)$$

and the field at the sites of the dipoles is again given by letting \mathbf{r} coincide in turn with the dipoles

$$\mathbf{E}(\mathbf{r}_j, \omega) = \mathbf{E}_0(\mathbf{r}_j, \omega) - \mu_0 \omega^2 \sum_{i \neq j}^N \alpha_i(\omega) \hat{\mathbf{G}}(\mathbf{r}_j, \mathbf{r}_i) \mathbf{E}(\mathbf{r}_i, \omega). \quad (2.53)$$

The main difference between the scalar model and the vectorial model is that the fields are vectors and the propagator is a tensor. To determine the field at the site of one of the dipoles Eqn. 2.53 is used. This equation is a set of N linear equations and as always such a set of equations can be written in matrix form. This can be easily seen if the set is written out for $N = 3$ for example. Eqn. 2.53 in matrix form looks like

$$(\hat{\mathbf{U}} + \hat{\mathbf{F}})^{-1} \mathbf{E}_0 = \mathbf{E}, \quad (2.54)$$

where \mathbf{E}_0 and \mathbf{E} are so called supervectors, because they are vectors of vectors, given by $\mathbf{E}_0 = \{\mathbf{E}_0(\mathbf{r}_1), \mathbf{E}_0(\mathbf{r}_2) \dots\}^T$, $\mathbf{E} = \{\mathbf{E}(\mathbf{r}_1), \mathbf{E}(\mathbf{r}_2) \dots\}^T$ and the interaction matrix $\hat{\mathbf{F}}$ is a supermatrix given by

$$\hat{\mathbf{F}} = \begin{pmatrix} \hat{0} & \mu_0 \omega^2 \alpha_2 \hat{\mathbf{G}}(\mathbf{r}_1, \mathbf{r}_2) & \mu_0 \omega^2 \alpha_3 \hat{\mathbf{G}}(\mathbf{r}_1, \mathbf{r}_3) & \dots \\ \mu_0 \omega^2 \alpha_1 \hat{\mathbf{G}}(\mathbf{r}_2, \mathbf{r}_1) & \hat{0} & \mu_0 \omega^2 \alpha_3 \hat{\mathbf{G}}(\mathbf{r}_2, \mathbf{r}_3) & \dots \\ \mu_0 \omega^2 \alpha_1 \hat{\mathbf{G}}(\mathbf{r}_3, \mathbf{r}_1) & \mu_0 \omega^2 \alpha_2 \hat{\mathbf{G}}(\mathbf{r}_3, \mathbf{r}_2) & \hat{0} & \dots \\ \dots & \dots & \dots & \dots \end{pmatrix}. \quad (2.55)$$

The matrix $\hat{\mathbf{F}}$ is called the interaction matrix because it describes how the incident field interacts with the dipoles. From Eqn. 2.54 it can be seen that when $\det[\hat{\mathbf{U}} + \hat{\mathbf{F}}] = 0$ the self consistent field becomes infinite. This is the resonance condition. For two dipoles located at $\mathbf{r}_1 = (0, 0, z)$ and $\mathbf{r}_2 = (0, 0, 0)$ the interaction matrix takes the form

$$\hat{\mathbf{F}} = \begin{pmatrix} \hat{0} & \mu_0 \omega^2 \alpha_2 \hat{\mathbf{G}}(\mathbf{r}_1, \mathbf{r}_2) \\ \mu_0 \omega^2 \alpha_1 \hat{\mathbf{G}}(\mathbf{r}_2, \mathbf{r}_1) & \hat{0} \end{pmatrix}. \quad (2.56)$$

This is a general expression in the sense that it still contains both direct and indirect contributions. Since the goal is to determine the resonance condition for two dipoles placed near each other the major contribution is from the near field direct propagator. Replacing $\hat{\mathbf{G}}$ by $\hat{\mathbf{D}}_{\text{nf}}$, expanding the propagator tensor and adding the unit tensor gives the following matrix

$$\hat{\mathbf{U}} + \hat{\mathbf{F}} = \begin{pmatrix} 1 & 0 & 0 & -\alpha_2/2\pi\epsilon_0 z & 0 & 0 \\ 0 & 1 & 0 & 0 & \alpha_2/4\pi\epsilon_0 z & 0 \\ 0 & 0 & 1 & 0 & 0 & \alpha_2/4\pi\epsilon_0 z \\ -\alpha_1/2\pi\epsilon_0 z & 0 & 0 & 1 & 0 & 0 \\ 0 & \alpha_1/4\pi\epsilon_0 z & 0 & 0 & 1 & 0 \\ 0 & 0 & \alpha_1/4\pi\epsilon_0 z & 0 & 0 & 1 \end{pmatrix}. \quad (2.57)$$

This expression is only valid for near fields, i.e. when the distance between the two dipoles in question obeys $kR \approx 0$. Equating the determinant of this matrix to 0 yields the resonance condition for a two dipole system

$$\left[1 - \frac{\alpha_1 \alpha_2}{16\pi^2 \varepsilon_0^2 R^6}\right]^2 \left[1 - \frac{\alpha_1 \alpha_2}{4\pi^2 \varepsilon_0^2 R^6}\right] = 0, \quad (2.58)$$

where z has been replaced by R because it is always possible to chose a coordinate system where one of the axes is parallel to the dipole axis. The type of resonance described by this equation is termed configurational resonance because for any value of the polarizabilities α_1 and α_2 there exists a value of R at which resonance occurs. In other words, resonance depends on the configuration of the dipoles.

Resonance can occur for both the x, y and z components of the field. The conditions for resonance in each component can be seen from Eqn. 2.58. The first factor corresponds to resonance in the x and y components. Thus, $\alpha_1 \alpha_2 / 16\pi^2 \varepsilon_0^2 R^6 = 1$ is the resonance condition for the x and y component. The condition is the same for both components because of symmetry. Similarly, the resonance condition for the z component is $\alpha_1 \alpha_2 / 4\pi^2 \varepsilon_0^2 R^6 = 1$. From this it can be seen that for resonance in the x and y components the dipoles have to be closer than for resonance in the z component.

2.4.2 Near Field of a Dipole

In this section the near field of an electric dipole will be treated. This field can be calculated by using the near-field direct propagator Eqn. 2.51. If an EM wave polarized in the x-direction is incident on a metal nanosphere the polarization of the nanosphere will be in the x-direction (for isotropic materials). Thus $\mathbf{E}_{\text{in}}(\mathbf{r}) = [E_{\text{in}}^x(\mathbf{r}), 0, 0]$ and

$$\mathbf{E}_{\text{sc}}(\mathbf{r}) = \frac{3\mu_0 c^2 \alpha(\omega)}{4\pi r^5} \left[x^2 - \frac{r^2}{3}, xy, xz \right] E_{\text{in}}^x(\mathbf{r}), \quad (2.59)$$

where the dipole has been placed at the origin. Consider the dipole field when moving along the x, y and z axes

$$\mathbf{E}_{\text{sc}}(x, 0, 0) = \frac{\mu_0 c^2 \alpha(\omega)}{4\pi x^5} [2x^2, 0, 0] \quad (2.60)$$

$$\mathbf{E}_{\text{sc}}(0, y, 0) = \frac{\mu_0 c^2 \alpha(\omega)}{4\pi y^5} [-y^2, 0, 0] \quad (2.61)$$

$$\mathbf{E}_{\text{sc}}(0, 0, z) = \frac{\mu_0 c^2 \alpha(\omega)}{4\pi z^5} [-z^2, 0, 0]. \quad (2.62)$$

From these equations it can be seen that the field is strongest along the polarization direction (non-radiative direction, a dipole does not radiate along it's axis) and that it is 180° out of phase with the field scattered perpendicular to the polarization direction.

In Fig. 2.10 the field of a dipole polarized along the x-axis is plotted. The field is considered in an x-y plane at $z=20$ nm. The main contribution to the total field when viewed from the x-y

plane at $z=20$ nm comes from the field component parallel to the polarization direction, as can be readily seen from Fig. 2.10(a). In this figure the x-component is plotted and it can be seen that the intensity is generally higher than in the other plots. This also means that the main contribution to the total intensity comes from the field component parallel to the polarization direction.

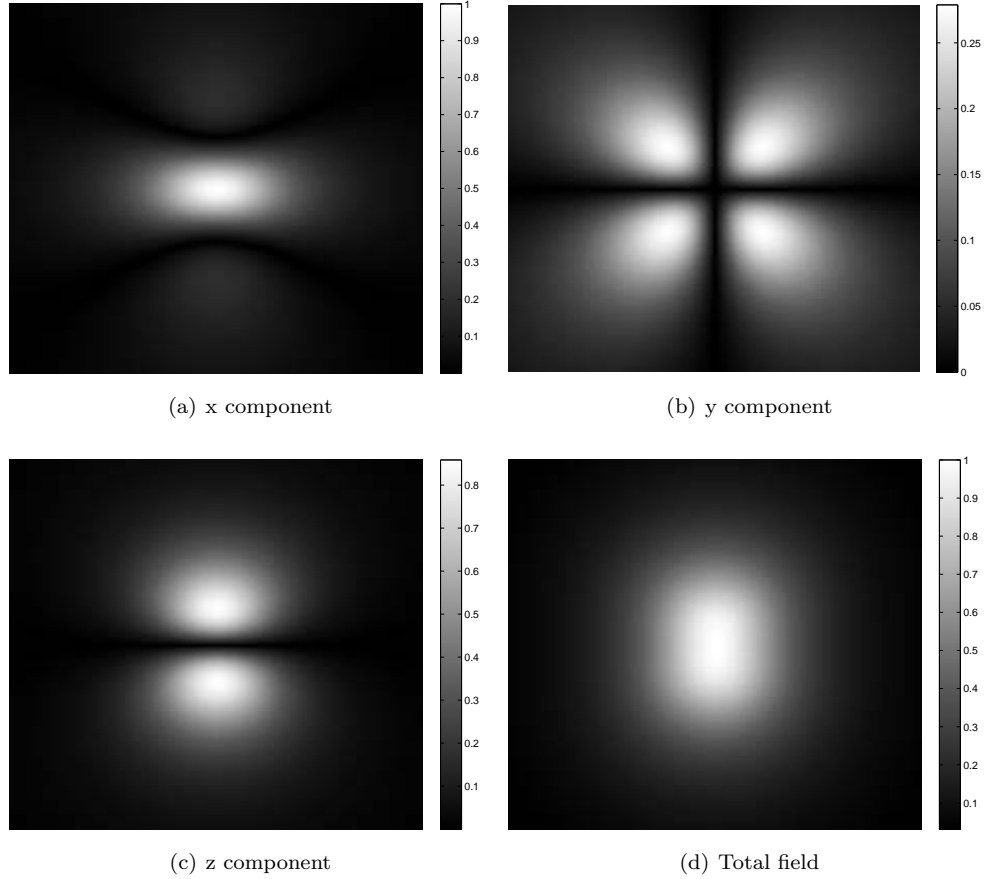


Figure 2.10: In this figure the components of the near-field of an electric dipole is shown. In all cases the polarization is along the x -axis. The dipole is being observed from an x - y plane at $z=20$ nm, x is horizontal in the figures and y is vertical, z is into the page. The total field refers to the magnitude of the electric field vector, ie. $\sqrt{(E_x^2 + E_y^2 + E_z^2)}$. The intensities have been normalized with respect to the maximum intensity, so that the intensity in all figures is relative to the maximum intensity. The image size is 100×100 nm.

2.4.3 Indirect Propagator

Where the direct propagator describes propagation of an EM wave from one dipole directly to another dipole, the indirect propagator describes the effect of having a surface near the two dipoles. In this case the EM wave scattered from one dipole will reflect off the surface and propagate from the surface to the other dipole. This suggests that the indirect propagator can

be written as the direct propagator with some factor taking into account the properties of the surface. The indirect propagator is given by [Keller et al., 1992]:

$$\hat{\mathbf{l}}_{\text{nf}}(\mathbf{r}, \mathbf{r}', \omega) = \hat{\mathbf{D}}_{\text{nf}}(\mathbf{r}, \mathbf{r}_M, \omega) \cdot \hat{\mathbf{M}}(\omega), \quad (2.63)$$

where the matrix $\hat{\mathbf{M}}$ is given by

$$\hat{\mathbf{M}}(\omega) = \frac{\varepsilon(\omega) - 1}{\varepsilon(\omega) + 1} \begin{pmatrix} -1 & 0 & 0 \\ 0 & -1 & 0 \\ 0 & 0 & 1 \end{pmatrix}. \quad (2.64)$$

The factor in front of the matrix is the nonretarded reflection coefficient for p-polarized light.

When a dipole is placed near a surface the EM radiation scattered from the dipole interacts with the dipole itself due to the reflection in the surface. This effect is called the surface dressing effect. Using the indirect propagator the field at the site of the dipole, taking into account the surface dressing effect, is given by

$$\mathbf{E}(\mathbf{r}_s) = \left[\hat{\mathbf{U}} + \mu_0 \omega^2 \alpha(\omega) \hat{\mathbf{l}}_{\text{nf}}(\mathbf{r}_s, \mathbf{r}_s) \right]^{-1} \cdot \mathbf{E}_0(\mathbf{r}_s). \quad (2.65)$$

The polarization of the dipole is determined by the field existing at the site of the dipole, ie. the self consistent field. Due to the surface dressing effect this field is not simply the incident field \mathbf{E}_0 . The polarization of the dipole is $\mathbf{P} = \hat{\alpha} \cdot \mathbf{E}(\mathbf{r}_s)$, thus

$$\mathbf{P} = \hat{\alpha}(\omega) \cdot \left[\hat{\mathbf{U}} + \mu_0 \omega^2 \alpha(\omega) \hat{\mathbf{l}}_{\text{nf}}(\mathbf{r}_s, \mathbf{r}_s) \right]^{-1} \cdot \mathbf{E}_0(\mathbf{r}_s), \quad (2.66)$$

and a new polarizability accounting for the surface dressing effect can be defined

$$\hat{\alpha}_{\text{sd}}(\omega) = \hat{\alpha}(\omega) \cdot \left[\hat{\mathbf{U}} + \mu_0 \omega^2 \alpha(\omega) \hat{\mathbf{l}}_{\text{nf}}(\mathbf{r}_s, \mathbf{r}_s) \right]^{-1}. \quad (2.67)$$

In this context it should be noted that contrary to the direct propagator the indirect propagator is defined for $R = 0$, because radiation from a dipole can couple to itself via the surface. As in the case of two dipoles it can be seen that for certain values of the interaction operator there exist resonances in the system. Resonances occur when $\det[\hat{\mathbf{U}} + \mu_0 \omega^2 \alpha(\omega) \hat{\mathbf{l}}_{\text{nf}}(\mathbf{r}_s, \mathbf{r}_s)] = 0$ corresponding to the condition

$$\left[\frac{\alpha(\omega) r^p(\omega)}{4\pi\epsilon_0 (2z)^3} - 1 \right]^2 \left[\frac{2\alpha(\omega) r^p(\omega)}{4\pi\epsilon_0 (2z)^3} - 1 \right] = 0, \quad (2.68)$$

where z is the distance of the dipole above the surface. As for the two dipole system resonances can occur in both the x, y and z components. Again, for resonance in the x and y components the dipole has to be closer to the surface than for the z component.

2.4.4 Relation to Surface Plasmon Polaritons

In this section the relation of the vectorial model to scattering of surface plasmon polaritons is described. Until now the propagation of EM radiation has been described by a direct and an indirect propagator without specifically separating out the contribution from SPPs. The propagation of EM fields by SPPs is contained within the indirect propagator together with the indirect propagation of s and p polarized waves. Separating the indirect propagator gives the following expression for the total propagator

$$\hat{G}(\mathbf{r}, \mathbf{r}') = \hat{D}(\mathbf{r}, \mathbf{r}') + \hat{I}^{\text{s-pol}}(\mathbf{r}, \mathbf{r}') + \hat{I}^{\text{p-pol}}(\mathbf{r}, \mathbf{r}') + \hat{G}_{\text{SPP}}(\mathbf{r}, \mathbf{r}'), \quad (2.69)$$

where the last term on the right hand side describes the propagation of SPPs. In Fig. 2.11 the different propagation paths are shown. The FF (far-field) indirect propagator is the propagation of EM radiation via reflection of s- and p- polarized EM waves in the surface. The SPP propagator is propagation via excitation of SPPs by near fields of the source dipole.

If both the source and the observation points are placed close to the surface and far from each other, the angle of incidence of the FF s- and p-polarized waves at the surface will be close to 90 degrees. Under these conditions the Fresnel reflection coefficients becomes approximately -1. This means that the two waves (the direct and the FF-indirect propagating ones) when they meet at the observation point will be approximately out of phase. Therefore the direct and FF-indirect part of the propagator does not contribute to the field at the observation point, and the total propagator is approximately given by

$$\hat{G}(\mathbf{r}, \mathbf{r}') \approx \hat{G}_{\text{SPP}}(\mathbf{r}, \mathbf{r}'). \quad (2.70)$$

This is an important result because it allows one to express the total propagator analytically. It is not possible to find an analytical expression for the indirect propagator but the SPP propagator can be described analytically. The SPP propagator is given in cylindrical coordinates by [Evlyukhin and Bozhevolnyi, 2005]

$$\hat{G}_{\text{SPP}}(\mathbf{r}, \mathbf{r}') = \frac{-iak_{\text{SPP}}H_0^{(1)}(k_{\text{SPP}}\rho)e^{-ak_{\text{SPP}}(z+z')}}{2(1-a^4)(1-a^2)} \times (\hat{z}\hat{z} + a^2\hat{\rho}\hat{\rho} + ia(\hat{z}\hat{\rho} - \hat{\rho}\hat{z})), \quad (2.71)$$

where $a = \sqrt{\varepsilon_r / -\varepsilon_m}$ and $\hat{\rho}$ and \hat{z} are cylindrical unit vectors. Using this the scattered field can be calculated.

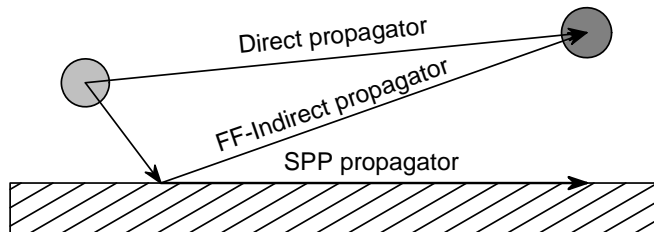


Figure 2.11: Direct and indirect propagation paths taking into account the scattering to SPPs. The SPP propagation path is shown along the surface since SPPs propagate along the surface.

2.4.5 Connection to Scalar Model

In this section the relation between the scalar model and the vectorial model will be established. In the scalar model only the z-component of the field was considered. In order to establish a connection between the two models, the z-component of the field is calculated in the framework of the vectorial model.

For scattering by a single particle, when both the observation point and the scatterer are placed near the surface and far from each other so that $\hat{\mathbf{G}} \approx \hat{\mathbf{G}}_{\text{SPP}}$, Eqn. 2.52 reduces to

$$\mathbf{E}(\mathbf{r}) = \mathbf{E}_0(\mathbf{r}) - \mu_0 \omega^2 \hat{\mathbf{G}}_{\text{SPP}}(\mathbf{r}, \mathbf{r}_p) \hat{\alpha}_{\text{sd}} \mathbf{E}_0(\mathbf{r}_p), \quad (2.72)$$

where the surface dressed polarizability has been introduced to take surface dressing into account. The scattered field is the last term on the right hand side of the equation. To proceed, an expression for $\hat{\alpha}_{\text{sd}}$ is needed. From Eqn. 2.67 the following expression can be obtained

$$\hat{\alpha}_{\text{sd}} = \alpha_0 \left(\frac{1}{1 + \xi\beta} \hat{\mathbf{x}}\hat{\mathbf{x}} + \frac{1}{1 + \xi\beta} \hat{\mathbf{y}}\hat{\mathbf{y}} + \frac{1}{1 + 2\xi\beta} \hat{\mathbf{z}}\hat{\mathbf{z}} \right) \quad (2.73)$$

$$\xi = \frac{(\varepsilon_r - \varepsilon_m)(\varepsilon_p - \varepsilon_r)}{(\varepsilon_r + \varepsilon_m)(\varepsilon_p + 2\varepsilon_r)} \quad (2.74)$$

$$\beta = \left(\frac{R_p}{2z_p} \right)^3. \quad (2.75)$$

The propagator should be written in rectangular coordinates. To do this the cylindrical unit vectors $\hat{\boldsymbol{\rho}}$, $\hat{\boldsymbol{\phi}}$ and $\hat{\mathbf{z}}$ are written in terms of $\hat{\mathbf{x}}$, $\hat{\mathbf{y}}$ and $\hat{\mathbf{z}}$

$$\hat{\boldsymbol{\rho}} = \cos \phi \hat{\mathbf{x}} + \sin \phi \hat{\mathbf{y}} + 0 \hat{\mathbf{z}} \quad (2.76)$$

$$\hat{\boldsymbol{\phi}} = -\sin \phi \hat{\mathbf{x}} + \cos \phi \hat{\mathbf{y}} + 0 \hat{\mathbf{z}}. \quad (2.77)$$

The unit vector $\hat{\mathbf{z}}$ is the same in both coordinate systems. The dyadic products can now be calculated

$$\hat{\boldsymbol{\rho}}\hat{\boldsymbol{\rho}} = \begin{pmatrix} \cos^2 \phi & \cos \phi \sin \phi & 0 \\ \sin \phi \cos \phi & \sin^2 \phi & 0 \\ 0 & 0 & 0 \end{pmatrix} \quad \hat{\mathbf{z}}\hat{\mathbf{z}} = \begin{pmatrix} 0 & 0 & 0 \\ 0 & 0 & 0 \\ 0 & 0 & 1 \end{pmatrix} \quad (2.78)$$

$$\hat{\mathbf{z}}\hat{\boldsymbol{\rho}} = \begin{pmatrix} 0 & 0 & 0 \\ 0 & 0 & 0 \\ \cos \phi & \sin \phi & 0 \end{pmatrix} \quad \hat{\boldsymbol{\rho}}\hat{\mathbf{z}} = \begin{pmatrix} \cos \phi & 0 & 0 \\ \sin \phi & 0 & 0 \\ 0 & 0 & 0 \end{pmatrix}. \quad (2.79)$$

Using this, the propagator assumes the form

$$\hat{\mathbf{G}}_{\text{SPP}}(\mathbf{r}, \mathbf{r}') = \frac{iak_{\text{SPP}}H_0^{(1)}(k_{\text{SPP}}\rho)e^{-ak_{\text{SPP}}(z+z')}}{2(1-a^4)(1-a^2)} \times \begin{pmatrix} a^2 \cos^2 \phi - ia \cos \phi & a^2 \cos \phi \sin \phi & 0 \\ a^2 \sin \phi \cos \phi - ia \sin \phi & a^2 \sin^2 \phi & 0 \\ ia \cos \phi & ia \sin \phi & 1 \end{pmatrix}. \quad (2.80)$$

The incoming SPP field can for $z > 0$ be described by [Evlyukhin and Bozhevolnyi, 2005]

$$\mathbf{E}_0(\mathbf{r}) = e^{ik_{\text{SPP}}x - ak_{\text{SPP}}z} (-ia, 0, 1). \quad (2.81)$$

From Eqn. 2.73, Eqn. 2.80 and Eqn. 2.81 the z-component of the scattered field can be calculated

$$E_{sc}^z(\mathbf{r}) = AH_0^{(1)}(k_{\text{SPP}}\rho) \frac{\alpha_0}{1 + 2\xi\beta} (1 + \eta_p \cos \phi) e^{-ak_{\text{SPP}}(z+2z_p)} \quad (2.82)$$

$$A = \frac{i\mu_0\omega^2 ak_{\text{SPP}}}{2(1-a^2)(1-a^4)} \quad (2.83)$$

$$\eta_p = \frac{a^2(1 + 2\xi\beta)}{1 + \xi\beta} \quad (2.84)$$

where the coordinate x has arbitrarily been set equal 0. It is now an easy matter to analytically evaluate the effective polarizability, introduced in the scalar model, subject to the condition $a \ll 1$. This is the condition for the validity of the scalar model, because the scalar model assumes the z-component of the field to be much larger than the x-component, and the parameter a determines the relationship between the x and z-component as seen from Eqn. 2.81. By equating the z-component of the scattered field in the two models under the condition $a \ll 1$, the effective polarizability is found to be

$$\alpha_e \approx \frac{6ak_0^3 V_p \varepsilon_r^{3/2} (\varepsilon_p - \varepsilon_r)}{\varepsilon_p + 2\varepsilon_r - 2\beta(\varepsilon_p - \varepsilon_r)}. \quad (2.85)$$

2.4.6 In Plane Scattering of SPPs

In the context of scattering of SPPs by nanoparticles, it is of interest to calculate the SPP to SPP scattering cross section in different in-plane directions. This makes it possible to determine in which directions the SPPs are scattered. To evaluate the scattering of SPPs to SPPs, the SPP to SPP scattering cross section is calculated. It is given by [Evlyukhin and Bozhevolnyi, 2005]

$$\sigma_{\text{SPP}}(\phi) d\phi = \frac{\int_{-\infty}^{\infty} \langle \mathbf{S}_{\text{SPP}} \rangle dz \rho d\phi}{\int_{y_1}^{y_2} \int_{-\infty}^{\infty} \langle \mathbf{S}_{\text{in}} \rangle dy dz / (y_2 - y_1)} \quad (2.86)$$

To evaluate this integral the denominator is first considered. The denominator integral represents the power (in the form of SPPs) incident on the scatterer. The integral is over all z below and above the surface. From [Evlyukhin and Bozhevolnyi, 2005] the field above the surface is given by

$$\mathbf{E}_0^> = e^{ik_{\text{SPP}}x - ak_{\text{SPP}}z} (-ia\hat{\mathbf{x}} + \hat{\mathbf{z}}) e^{i\omega t}, \quad z > 0 \quad (2.87)$$

Where the $>$ sign is meant to indicate that z is larger than zero. From the boundary conditions and the requirement that the divergence of the field has to be zero inside the surface, the field inside the surface can be calculated. It is assumed that the field inside the surface has the same propagation constant along x as the field outside the surface so that the field inside has the form $\mathbf{E}_0^< = e^{ik_{\text{SPP}}x + C_3z} (C_1\hat{\mathbf{x}} + C_2\hat{\mathbf{z}}) e^{i\omega t}$

$$C_1 = -ia \quad (2.88)$$

$$C_2 = \frac{\varepsilon_r}{\varepsilon_m} \quad (2.89)$$

$$C_3 = iC_1k_{\text{SPP}}/C_2 = ak_{\text{SPP}}\varepsilon_m/\varepsilon_r = -k_{\text{SPP}}/a \quad (2.90)$$

since $\varepsilon_m/\varepsilon_r = -1/a^2$. Thus, the field inside the surface is given by

$$\mathbf{E}_0^< = -a^2 e^{ik_{\text{SPP}}x - k_{\text{SPP}}z/a} (i/a\hat{\mathbf{x}} + \hat{\mathbf{z}}) e^{i\omega t}, \quad z < 0 \quad (2.91)$$

The magnitude of the electric field inside the surface is determined by a so that the field inside the surface becomes small when a becomes small. Inside the surface the z -component is smaller than the x -component since $a < 1$ (the opposite is true above the surface). This is because the x -component is preserved across the surface due to the boundary conditions, whereas the z -component is not.

To calculate the poynting vector the magnetic fields are needed. These are calculated from Faradays induction law, $\nabla \times \mathbf{E} = -\mu_0 \frac{d\mathbf{H}}{dt}$ (non magnetic media) and are given by the two expressions

$$\mathbf{H}_0^> = \frac{k_{\text{SPP}}}{\omega} (1 - a^2) e^{ik_{\text{SPP}}x - ak_{\text{SPP}}z} e^{i\omega t} \hat{\mathbf{y}} \quad (2.92)$$

$$\mathbf{H}_0^< = \frac{k_{\text{SPP}}}{\omega} (1 - a^2) e^{ik_{\text{SPP}}x + k_{\text{SPP}}z/a} e^{i\omega t} \hat{\mathbf{y}} \quad (2.93)$$

The magnetic field inside and outside are equal for all x at $z=0$ which of course has to be true in order to fulfil the boundary conditions. Now the poynting vectors above and below the surface can be calculated from $\mathbf{S} = \mathbf{E} \times \mathbf{H}$. Before calculating the poynting vector it is necessary to take the real part of the fields because the poynting vector is non linear in the fields so that it is no longer justified to use the complex exponential notation. Mathematically, the justification for using complex exponential notation is that the Maxwell equations are linear so that both the real and the imaginary part of the complex fields are solutions. Above the surface the poynting vector is given by

$$\begin{aligned}
\langle \mathbf{S}_{\text{in}}^> \rangle &= \left\langle \frac{k_{\text{SPP}}}{\mu_0 \omega} (a^2 - 1) e^{-2ak_{\text{SPP}}z} \cos^2(k_{\text{SPP}}x + \omega t) \right\rangle \hat{\mathbf{x}} \\
&\quad + \left\langle \frac{ak_{\text{SPP}}}{\mu_0 \omega} (1 - a^2) e^{-2ak_{\text{SPP}}z} \sin(k_{\text{SPP}}x + \omega t) \cos(k_{\text{SPP}}x + \omega t) \right\rangle \hat{\mathbf{y}} \\
&= \frac{k_{\text{SPP}}}{2\mu_0 \omega} (a^2 - 1) e^{-2ak_{\text{SPP}}z} \hat{\mathbf{x}}
\end{aligned} \tag{2.94}$$

since the time average of the y component is zero. Below the surface the poynting vector is

$$\begin{aligned}
\langle \mathbf{S}_{\text{in}}^< \rangle &= \left\langle \frac{-a^4 k_{\text{SPP}}}{\mu_0 \omega} \left(\frac{1}{a^2} - 1 \right) e^{2k_{\text{SPP}}z/a} \cos^2(k_{\text{SPP}}x + \omega t) \right\rangle \hat{\mathbf{x}} \\
&\quad + \left\langle \frac{a^4 k_{\text{SPP}}}{\mu_0 \omega a} \left(\frac{1}{a^2} - 1 \right) e^{2k_{\text{SPP}}z/a} \sin(k_{\text{SPP}}x + \omega t) \cos(k_{\text{SPP}}x + \omega t) \right\rangle \hat{\mathbf{y}} \\
&= \frac{-a^4 k_{\text{SPP}}}{2\mu_0 \omega} \left(\frac{1}{a^2} - 1 \right) e^{2k_{\text{SPP}}z/a} \hat{\mathbf{x}}
\end{aligned} \tag{2.95}$$

By integrating these expressions according to Eqn. 2.86 the following expression for the incident power is obtained

$$P_{\text{in}} = \frac{1}{2k_0} \sqrt{\frac{\varepsilon_0}{\mu_0}} \frac{1 - a^2}{2a} (1 - a^4) \tag{2.96}$$

By doing the same calculation but with the field above the surface only, the same result without the $-a^4$ term is obtained. This shows that the $-a^4$ term stems from the flux of energy below the surface, and that the energy flux can be concentrated above the surface by making $-\varepsilon_m$ significantly larger than ε_r . The numerator of Eqn. 2.86 can be calculated by a procedure similar to the one just shown. The scattered field is first determined, then the magnetic field, and the poynting vector can then be calculated and averaged in time. The calculation is not made here. The result is [Evlyukhin and Bozhevolnyi, 2005]

$$\langle \mathbf{S}_{\text{SPP}} \rangle = \frac{1}{k_0} \sqrt{\frac{\varepsilon_0}{\mu_0}} |A|^2 \left(\frac{\alpha_0}{1 + 2\xi\beta} \right)^2 e^{-2ak_{\text{SPP}}(z+2z_p)} \frac{(1 + \eta_p \cos \phi)^2 (1 - a^2)}{\pi \rho} \tag{2.97}$$

By carrying out the integration and using Eqn. 2.86 the scattering cross section becomes

$$\sigma_{\text{SPP}}(\phi) d\phi = 2 |A|^2 \left(\frac{\alpha_0}{1 + 2\xi\beta} \right)^2 \frac{(1 + \eta_p \cos \phi)^2}{\pi k_{\text{SPP}}} e^{-4ak_{\text{SPP}}z_p} \tag{2.98}$$

From this expression it is seen that the cross section decays exponentially as the scatterer-surface distance z_p increases. This makes good sense because the SPP field decreases exponentially away from the surface into the dielectric, so that the scattering will also decrease exponentially. The angular dependence of the scattering cross section is determined by $(1 + \eta_p \cos \phi)$

so that the scattering is most powerful in the $\phi = 0$ direction, ie. the direction of the incident plasmon. From the expression Eqn. 2.84 for η_p and Eqn. 2.75 for β it can also be seen that the angular dependence is depressed when the particle is moved away from the surface (if $a \ll 1$).

In Fig. 2.12 the scattering cross section is plotted for a nanoparticle of radius 10 nm placed in different distances from the surface. The cross section becomes smaller and the angular dependence is depressed when the particle-surface distance increases, as discussed above.

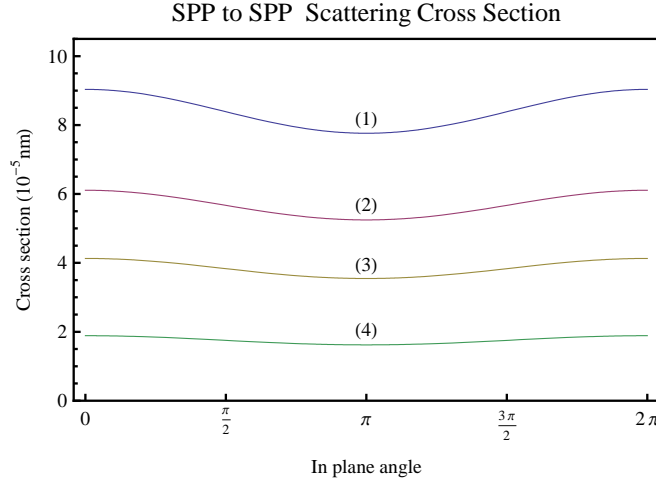


Figure 2.12: In-plane SPP to SPP scattering cross section in different directions and with different particle-surface distances. (1) 50 nm, (2) 100 nm, (3) 150 nm, (4) 250 nm. The light wavelength is 638 nm and the particle radius is 10 nm.

Chapter 3

Numerical Results

Contents

3.1	Scalar Model Results	39
3.1.1	Single Particle Scattering	39
3.1.2	Mirrors	40
3.1.3	Waveguides	40
3.2	Vectorial Model Results	41
3.2.1	Scalar Model and Vectorial Model Comparison	42
3.2.2	Parabolic Nanoparticle Chains for SPP Beam Focusing	43

In this chapter the results from the simulations are presented and discussed. Simulations of different types of structures are made using both the vector model and the scalar model and some of the differences between the models are described.

3.1 Scalar Model Results

This section presents the results from the numerical calculations based on the scalar model described in Sec. 2.2. The results are shown in Fig. 3.1 through Fig. 3.3. In all images the origin of the coordinate system lies in the middle of the image. The positive x-axis is to the right and the positive y-axis is up. In all cases the SPP is incident from the left.

3.1.1 Single Particle Scattering

In Fig. 3.1 the simulation of single particle scattering of SPPs is shown. This image should be compared to Fig. 2.8(c) where the high intensity fringes are calculated analytically. The two images of course correspond to each other, since they are manifestations of the same theory. Fig. 3.1(a) shows the same single particle scattering for a gaussian beam. The same features are replicated in this image. In Fig. 3.1(b) the scattering of a plane wave is shown. The bending of the phase fronts are in both cases due to interference between the incident plane wave and the scattered isotropic cylindrical wave.

Near the scatterer the phase fronts are very clear but far left from the scatterer they become less clear. This is because the intensity of the scattered wave decreases as $1/r$ where r is the

distance from the scatterer. Far from the scatterer thus, the scattered wave is very weak and no interference between the incident and scattered waves is observed. On the right side of the scatterer, along the line $(x > 0, 0)$, the intensity is seen to be equally distributed with no interference patterns. This different behaviour on the left and right sides of the scatterer can be easily understood by considering a plane wave propagating along $+x$ (wave scattered to the right) and one propagating along $-x$ (wave scattered to the left). The incident beam also propagates along $+x$, thus:

$$I_{\text{left}}(x) = \left| e^{ix} + \frac{1}{\sqrt{x}} e^{i(-x+\pi/2)} \right|^2 = 1 + \frac{1}{x} + \frac{2}{\sqrt{x}} \sin 2x \quad (3.1)$$

$$I_{\text{right}}(x) = \left| e^{ix} + \frac{1}{\sqrt{x}} e^{i(x+\pi/2)} \right|^2 = 1 + \frac{1}{x} \quad (3.2)$$

where the phase shift $\pi/2$ stems from the fact that the scattered wave is 90° out of phase with the incident wave. From this it is seen that on the left side of the scatterer the intensity is an oscillatory function of x , but on the right side it is proportional to $1/x$.

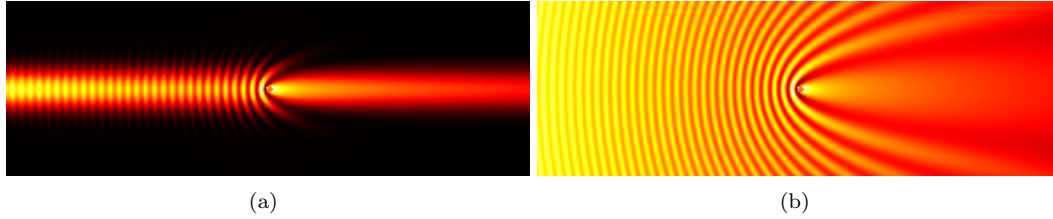


Figure 3.1: Numerical results from the scalar model showing single particle scattering. (a) the incident SPP is described by a gaussian wave, in (b) the SPP is described by a plane wave. In both cases the SPP is incident from the left.

3.1.2 Mirrors

By placing arrays of nanoparticles on the surface, mirror structures capable of reflecting SPPs can be created. These structures are illustrated in Fig. 3.2. In both figures the wavelength of the incident SPP is 700 nm and the SPP is incident from the left. The difference between the pictures is the lattice constant of the mirror structure. In Fig. 3.2(a) the lattice constant is 700 nm, i.e., the same as the wavelength. It is seen that the mirror is very leaky. Much of the incident radiation is transmitted through the mirror, and not so much is reflected. In Fig. 3.2(b) on the other hand, the lattice constant is 200 nm, smaller than the wavelength. Here it is seen that the SPP is reflected, and that the angle of incidence seems to equal the angle of reflection. Most of the intensity is reflected and seemingly only a small fraction is backscattered or transmitted.

3.1.3 Waveguides

When an SPP is incident on a large periodic array of scatterers (on the order of 20×20 scatterers) the propagation of the SPP is determined by its wavelength and the configuration of the

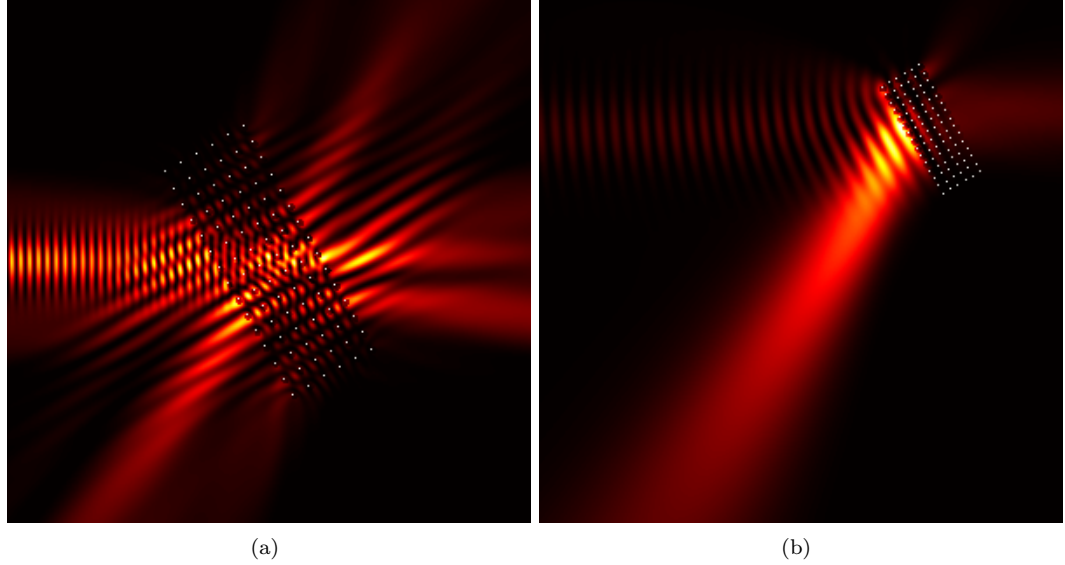


Figure 3.2: Numerical results from the scalar model showing reflection of SPPs off a mirror structure. In both images the SPP is incident from the left with a wavelength of 700 nm. Fig. 3.2(a) is a mirror structure with lattice constant 700 nm, and Fig. 3.2(b) is a mirror structure with lattice constant 200 nm.

scatterers. For certain combinations of SPP wavelength and configuration of scatterers, SPP propagation is inhibited inside the array. In Fig. 3.3(a) a periodic array of 20×30 scatters with a scatterer distance of 300 nm is shown. The plasmon is incident from the left with a wavelength of 685 nm. It is seen that the array block SPP propagation, the intensity on the right side of the array is very weak. The SPP is almost completely reflected and the intensity decreases inside and along the array. In Fig. 3.3(b) the same structure is shown but with three rows missing. Here it is seen that there is still a large reflection, but that SPPs are also guided through the channel. The highest intensity is found just outside the end of the channel.

For the waveguide to guide the light only through the channels, it is necessary that the wavelength of the incident SPP lies somewhere in the SPP bandgap (SPPBG) of the array. If this is not the case, the SPP will propagate through and inside the structure even if there are no missing rows.

3.2 Vectorial Model Results

In the last section the results from the scalar model were presented. In this section the results from the vectorial model are shown. The results are based on the theory described in Sec. 2.4. As in the last section all images have the origin in the middle of the image, the positive x-axis is directed to the right and the positive y-axis is directed upwards. In all images the SPP is incident from the left.

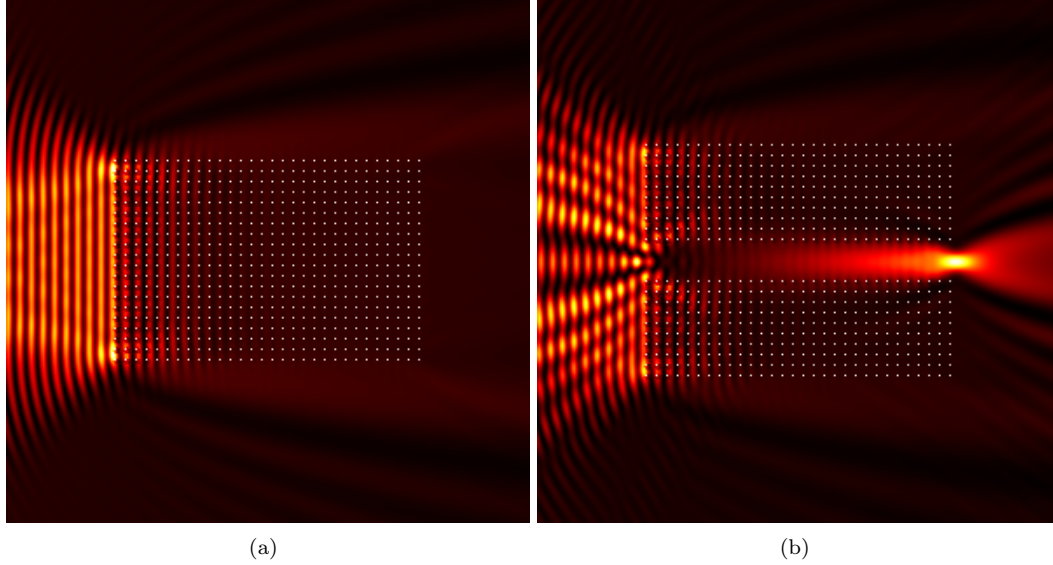


Figure 3.3: Numerical results from the scalar model showing how columns of nano particles can inhibit the SPP propagation. When some rows are missing the SPP is guided through the channel. In both images the SPP (described by a plane wave) is incident from the left. The wavelength of the SPP is 685 nm and the lattice constant of the arrays is 300 nm. The array contains 30×20 scatterers. The image represents an area of $15\mu\text{m} \times 15\mu\text{m}$.

3.2.1 Scalar Model and Vectorial Model Comparison

In Fig. 3.4(a) single scattering is simulated using the scalar model and in Fig. 3.4(b) the same scenario is simulated using the vectorial model. It is seen that the two models give almost identical images. Careful investigation of the images shows a slightly higher intensity in the scalar model than in the vectorial model. This small difference can be attributed to the fact that the vectorial model takes into account the x- and y-component of the field so that all the radiation power is not concentrated in the z-component, as is assumed in the scalar model. Fig. 3.4(c) and Fig. 3.4(d) shows the x- and y- component of the field respectively. In this simulation the x-component is smaller than the z-component by two orders of magnitude and the y-component is smaller by four orders of magnitude, so that to a very good approximation all the power is concentrated in the z-component.

The y-component of the field is zero along the line $\phi = 0$ and maximum along $\phi = \pi/2$. This can be readily seen from the form Eqn. 2.80 of the propagator. The y-component of the field is related to the second row of the matrix, and this row contains all zeros at $\phi = 0$. It should be noted that the fields shown in Fig. 3.4 are not the scattered fields, they are the scattered field plus the incident field, according to Eqn. 2.52. This is why the y-component does not display any interference pattern. There is no incident field for the y-component to interfere with. It is also the reason why the x-component is almost constant over the area shown. The x-component of the scattered field is of the same order of magnitude as the y-component, so that the main contribution to the intensity in Fig. 3.4(c) stems from the incident field. Actually, the x-component of the scattered field looks similar to the y-component except for being rotated 90° about the scatterer.

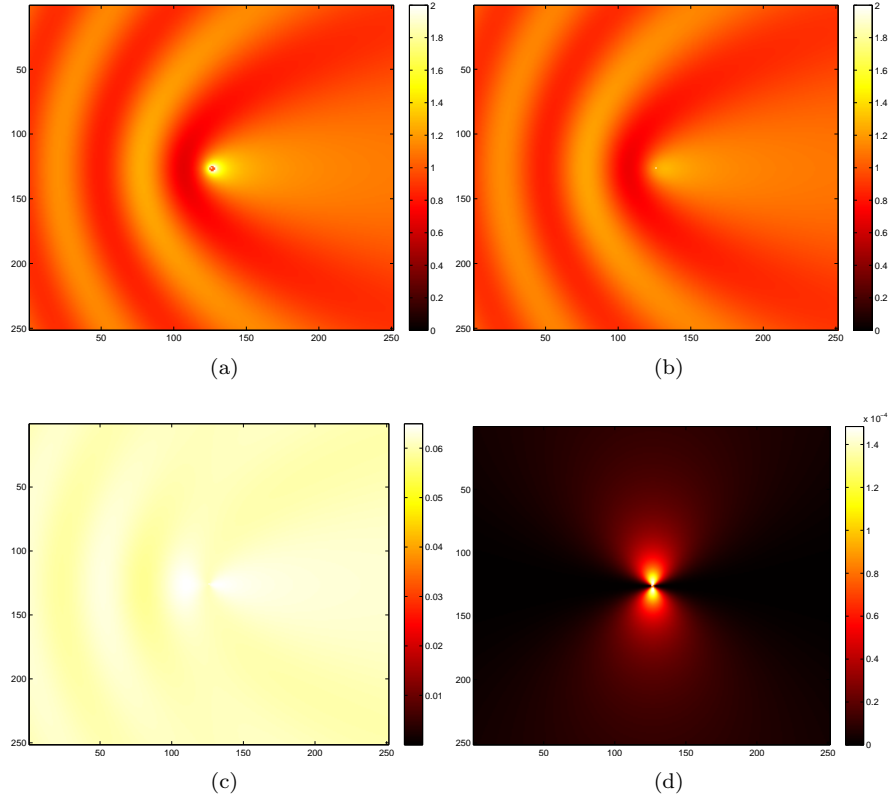


Figure 3.4: Simulation of single particle scattering in both the scalar and the vectorial model. (a) is calculated using the scalar model, (b), (c) and (d) are the z , x and y component of the field using the vectorial model, respectively. Parameters of the simulations are $\lambda = 700$ nm, $\varepsilon_m = \varepsilon_p = -16.5$, $\varepsilon_r = 1$, $R_p = 50$ nm.

3.2.2 Parabolic Nanoparticle Chains for SPP Beam Focusing

By directing an SPP beam towards the opening of a parabolic chain of nanoparticles the SPP beam can be focused into a small point. The nanoparticles are placed on the parabola with a constant distance between them. The properties of the beam focusing are determined by the width of the parabola at the opening, the height of the parabola and the distance between scatterers. The focal distance of the parabola can be determined by the following expression

$$\text{FD} = \frac{-w^2}{16h} \quad (3.3)$$

where h is the height of the parabola and w is the width of the parabola as defined by $y(-w/2) = y(w/2) = -h$ where $y(x) = ax^2$ is the expression for the parabola. From this expression it is seen that the focal distance is negative since h (and w) is a positive number. Since the parabola has its apex at the origin this means that the focal point lies within the parabola.

In Tbl. 3.1 focal distances for a number of combinations of parabola widths and heights are

w (nm) / h (nm)	4000	8500	10000	12000	16000
20000	-50	-225	-312	-505	-800
30000	-34	-150	-208	-300	-534
40000	-25	-112	-156	-225	-400
50000	-20	-90 ^(a)	-125 ^(b)	-180 ^(c)	-320
60000	-17	-75	-104	-150	-267

Table 3.1: Focal distances (in nm) for different combinations of parabola width and height. The widths are listed horizontally and the heights are listed vertically. The focal distances are negative which means that the focal point is positioned within the parabola. The letters in parentheses are used as reference to the parabolas in the images below.

shown. For the focal distance to be large in comparison with the parabola dimensions the parabola should be wide and the height should be small. This however will result in poor SPP focusing because the parabola branches are only good reflectors at oblique incidence [Evlyukhin et al., 2006] [Radko et al., 2007]. Therefore the width and height should be chosen so that the ratio w^2/h is small and the focal distance will consequently lie in the lower left part of the table. The letters (a), (b) and (c) in the table are used to designate the three different parabolas which have been used in the simulations and the experiments. They are used for reference later.

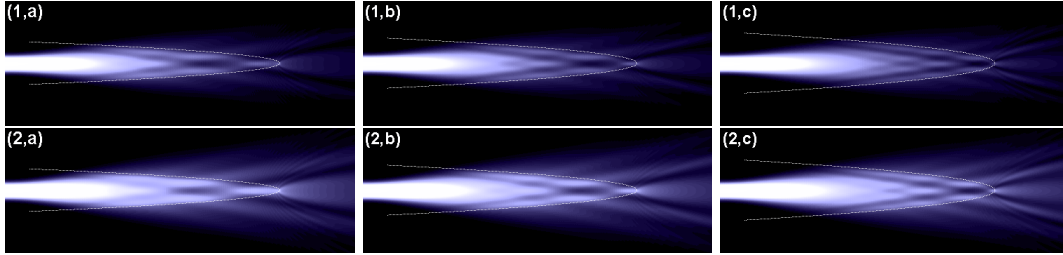


Figure 3.5: Simulation of SPPs incident on parabolic chains of nanoparticles. In all images the spacing between the particles is 281 nm. In the first row the excitation wavelength is 750 nm and in the second it is 855 nm. The first column is for parabolas with a width of 8.5 μm , the second 10 μm and the third 12 μm ie. (a), (b) and (c) as according to Tbl. 3.1.

In Fig. 3.5 simulations of parabolas (a) to (c) are shown for wavelengths 750 nm and 855 nm. The left column is parabola (a), the middle is parabola (b) and the last is parabola (c). The first row is for excitation wavelength of 750 nm and the second row is for excitation wavelength of 855 nm. All images in the figure are for nanoparticle spacings of 281 nm. In Fig. 3.6 the same images are shown but for nanoparticle spacings of 322 nm. All images are of dimensions $70 \times 20 \mu\text{m}$ and the beam waist was in all cases set to 1.5 μm . The height of all parabolas is 50 μm .

From the images it is seen that the parabolic structure focus the divergent SPP beam in a point near the apex of the parabola as expected from the calculation of the focal distance. The focusing is more apparent for parabolas of type (c) opening width than for the parabolas of smaller opening width. The interference patterns seen are believed to be interference between the original SPP beam and the SPP beam reflecting off the parabola branches. In the images it is seen that the SPP propagation length increases when the wavelength increases.

There is not seen any obvious difference between the parabolas with 322 nm nanoparticle

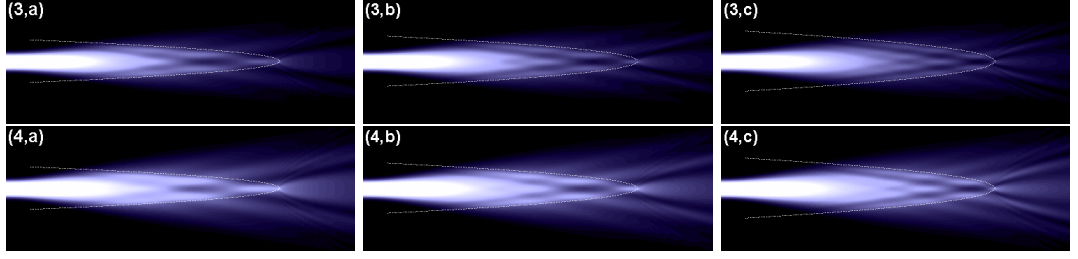


Figure 3.6: Simulation of SPPs incident on parabolic chains of nanoparticles. In all images the spacing between the particles is 322 nm. In the first row the excitation wavelength is 750 nm and in the second it is 855 nm. The first column is for parabolas with a width of 8.5 μm , the second 10 μm and the third 12 μm ie. (a), (b) and (c) as according to Tbl. 3.1.

spacing and those with 281 nm spacing. To investigate the effect of nanoparticle spacing simulations of parabolic chains with spacings 100 nm, 500 nm and 700 nm have been made. The parabolas are all of type (c) and they are shown in Fig. 3.7. From these images it is clearly seen that when the spacing decreases the interference patterns inside the parabolas become clearer. In the case of 500 nm spacing the pattern is smeared out. This smearing out is even more apparent in the case of 700 nm spacing.

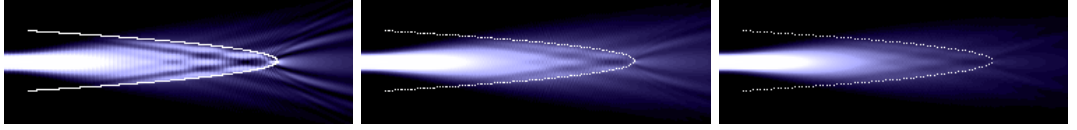


Figure 3.7: Simulations of SPPs incident on parabolas with nanoparticle spacings of 100 nm, 500 nm and 700 nm. Wavelength is 855 nm, parabola width is 12000 nm. All parabolas in this figure are of type (c).

Chapter 4

Experimental Setup

Contents

4.1	ATR Setup	47
4.2	LRM Setup	48

In this chapter the experimental setups are described along with the principle behind leakage radiation microscopy and the Fourier filter.

4.1 ATR Setup

In Fig. 4.1 the setup for measuring the laser beam reflection from the gold film on the prism as a function of incident angle is shown. The setup consists of two polarizers, a laser and two coincident circular disks connected to a step motor through two rubber bands.

The smaller of the two disks is placed below the other as shown by the dashed circle in the figure. Because the inner disk is half the circumference of the other the rotation speed of the inner disk is twice that of the outer disk. Because the detector is mounted on the inner disk and the prism is placed on top of the outer disk, the rotation speed of the detector is twice that of the prism. This is necessary because when the prism has rotated an angle of e.g. 45° the reflected beam has rotated an angle of 90° . If the detector does not rotate twice the speed of the prism the reflected beam will only hit the detector in the very beginning of the experiment.

The laser used in the experiment was a HeNe laser at a wavelength of 632 nm. The two polarizers in the setup are to enable control of the intensity of the incident light, but also to be able to exclude p-polarized light in order to check whether the observations are really due to SPPs.

The experiments were made by first positioning the prism so that the laser hits the gold film at an angle of 45° (Fig. 4.2(B)). The prism was then rotated clockwise about 5° so that the setup reaches the position shown in Fig. 4.2(A). From this position the experiment starts and the prism is rotated until the position shown in (C) is reached, with the reflection being recorded and saved for each step. 3600 steps corresponds to 90° rotation so that the $\sim 10^\circ$ rotation results in ~ 400 data points, enough to obtain an acceptable resolution.

It is important that the laser beam hits the gold film at the position which is exactly above

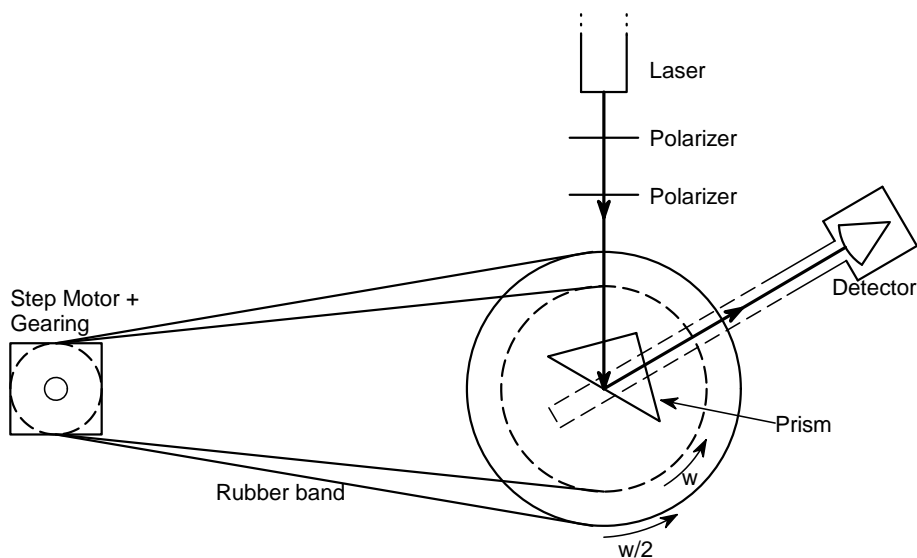


Figure 4.1: Sketch of the setup for measuring the SPP excitation angle. Two polarizers are placed immediately after the laser in order to be able to control the incident radiation. The prism is placed on one of two coincident disks rotating with different angular velocities as shown. The rotation is driven by a step motor. The prism is coated with a gold film on one of its sides.

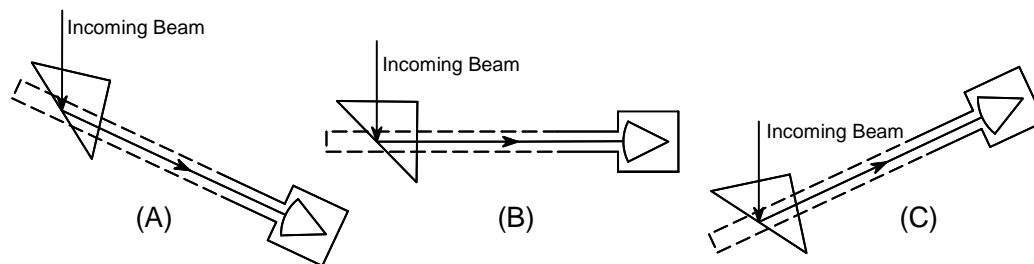


Figure 4.2: This figure shows the rotation of the detector. (A) is the first position and (C) is the last position.

the center of the disk. If it does not do so the laser reflection beam will not move with the detector and the two will get out of alignment.

4.2 LRM Setup

As described in the introduction leakage radiation microscopy is a way to image the fields from SPPs. The SPPs are excited on a gold surface on the sample by a focused laser beam hitting a gold ridge. The laser used in the experiments is a pumped Titanium Sapphire laser with adjustable wavelength in the range 700 nm - 860 nm. The setup used to map the SPP fields in the experiments is sketched in Fig. 4.3.

Two polarizers are placed immediately after the laser. These are used to control the intensity of the laser beam while still keeping the beam p-polarized. By adjusting the second polarizer

s-polarized light can be blocked and by adjusting the first one the intensity of p-polarized light can be controlled. In this way purely p-polarized light with adjustable intensity is sent to the sample.

Before the laser beam enters objective 1 it passes through a beam splitter. At this point a lamp is placed making it possible to expose the sample by white light. This is necessary to visualize the structures on the sample and thereby for pointing out the position for SPP excitation. The sample is moved by an XYZ stage driven by three piezoelectric motors.

The beam is focused on the metal surface by objective 1 and SPPs are excited and emits radiation in a narrow range around a characteristic angle θ_{LR} . At this angle the relation $k_{\text{SPP}} = 2\pi/\lambda_{\text{SPP}} = nk_0 \sin \theta_{\text{LR}}$ is satisfied, where λ_{SPP} is the SPP wavelength, n is the refractive index of the glass substrate, and k_0 is the modulus of the free space light wavevector. Because the angle is higher than the critical angle the emitted radiation will be totally reflected when it hits the glass substrate and will therefore never reach objective 2. Therefore an immersion fluid with refractive index equal to that of the glass substrate is placed between the glass substrate and objective 2. Objective 2 has a numerical aperture $\text{NA} > 1$ in order to collect the light.

Not only the leakage radiation enters objective 2, but also some direct radiation penetrates the sample and enters the objective. This direct radiation leads to strong overexposure of the CCD camera at the position of the laser beam. This strong radiation can be removed by using a Fourier filter [Drezet et al., 2006]. The principle is to project the Fourier plane onto a filter which removes the non-propagating (in the x-y plane) components. The propagating components corresponding to SPPs are seen in the Fourier plane as two lines opposite each other on the circumference of a circle with radius k_{SPP} . The non-propagating components corresponding to the direct radiation is seen in the Fourier plane as a bright spot in the center. By blocking this bright spot the direct radiation can be removed from the image plane so as to avoid overexposure of the CCD camera and thereby obtain better contrast. The Fourier plane of the radiation is projected by lens 1 on the Fourier filter where the radiation intensity is selectively blocked preventing further propagation of the direct radiation.

The sample used was fabricated on a glass substrate by e-beam lithography and a following liftoff process. A gold ridge is formed at the opening of the parabolic chains of gold nanoparticles allowing for excitation of SPPs. Several different parabolas were fabricated on the same sample.

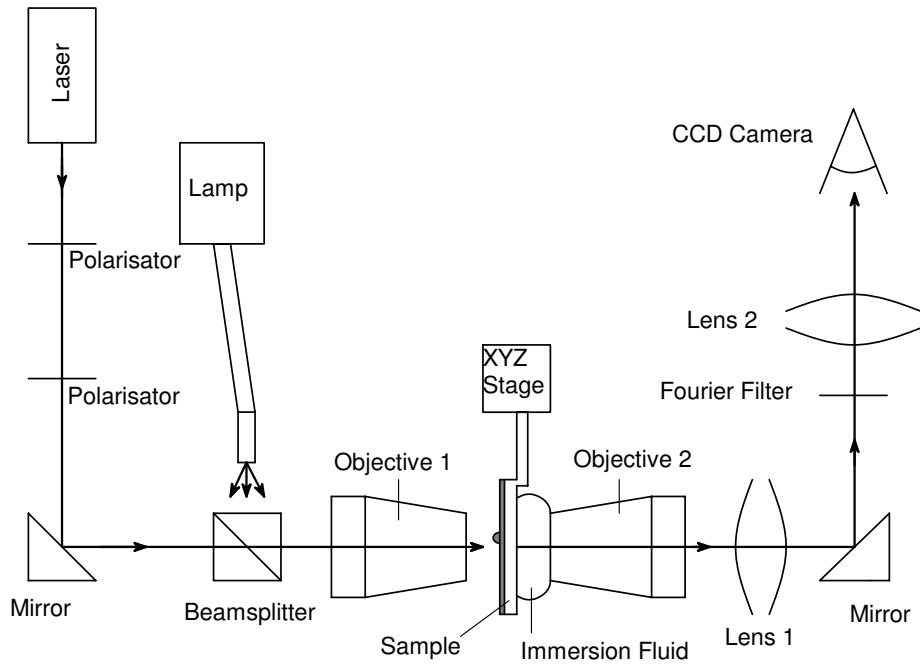


Figure 4.3: Sketch of the setup used in the LRM experiments. When the beam emerge from the laser it propagates through two polarizers before it enters objective 1 and is focused on the metal surface on the sample. An XYZ stage is controlling the position of the sample, making it possible to control the point at which the SPPs are excited. The SPP field radiates through the sample and the immersion fluid and enters the high NA objective 2. The image of the fields is magnified and send through a Fourier filter to remove the direct radiation before it is recorded by the CCD camera.

Chapter 5

Experimental Results and Discussion

Contents

5.1	ATR Results	51
5.1.1	Data Fitting	52
5.2	LRM Results	53
5.2.1	Propagation Length	55
5.2.2	Parabola Shape and Particle Spacing	56
5.2.3	Shape of the SPP Beam	57
5.2.4	Comparison Between Numerical Results and Experiments	57

This chapter presents and dicusses the experimentally obtained images and reflection intensity curves. The results are compared to the theory and the validity of the theoretical models is discussed.

5.1 ATR Results

The reflection data achieved from the experiments are measured as a function of the incoming angle at the air/prism interface. To compare these results with theory, a conversion factor is needed to convert the measured angle, θ_i , to the incoming angle at the prism/gold interface, θ . The geometry of the prism is sketched on Fig. 5.1.

At the air/prism interface the light is transmitted through the interface at an angle of θ_t . This angle can be calculated by Snell's law, thus

$$\theta_t = \arcsin \frac{n_a \sin \theta_i}{n_p}. \quad (5.1)$$

The angle α_1 is now given as $\alpha_1 = \pi/2 \pm \theta_t$, where + is used when light enters the prism from the side marked + (below the prism-air normal) on Fig. 5.1 and – is used when light

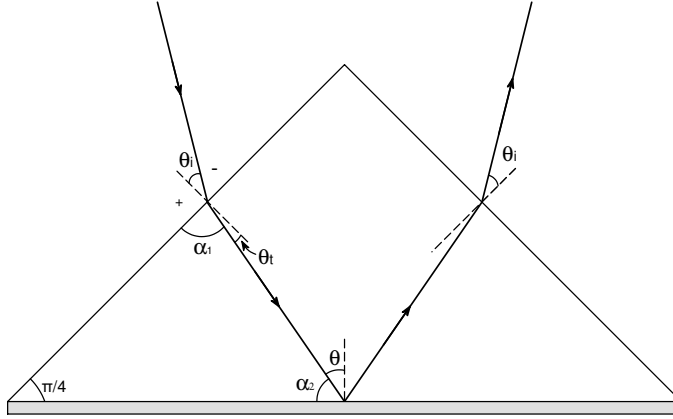


Figure 5.1: Geometry of the prism in the setup. Light impinges the air/prism interface at an angle of θ_i and is transmitted through the interface at an angle of θ_t . Inside the prism light impinges the prism/metal interface at an angle of θ .

enters the prism from the side marked $-$ (above the normal). The angle α_2 can be expressed as $\alpha_2 = \pi - \pi/4 - \alpha_1$. It is now possible to write the dependence of θ on θ_i as

$$\theta = \frac{\pi}{2} - \alpha_2 \quad (5.2)$$

$$= \frac{\pi}{2} - \left(\pi - \frac{\pi}{4} - \left(\frac{\pi}{2} \pm \arcsin \frac{n_a \sin \theta_i}{n_p} \right) \right) \quad (5.3)$$

$$\theta = \frac{\pi}{4} \pm \arcsin \frac{n_a \sin \theta_i}{n_p}. \quad (5.4)$$

5.1.1 Data Fitting

In the theory chapter an expression for the reflection intensity of a two interface system was deduced, Eqn. 2.23. This expression can be fitted to the achieved data from the SPP excitation experiments. In the experiments the thickness d and the permittivity $\varepsilon' + i\varepsilon''$ of the metal layer are not known exactly. These factors are therefore used as fitting parameters. To compensate for potential offset errors in the measured angles, an additional fitting parameter, θ_0 , is added. The deduced equation for the reflection intensity, Eqn. 2.23, therefore becomes a function of $\theta + \theta_0$. Furthermore, since the intensity in the experiments is not normalized the expression for the reflection intensity is multiplied by a fitting parameter I_0 so that the fitted reflection intensity can reach values larger than unity. The equation used to fit the data now becomes

$$R(\theta + \theta_0) = I_0 \left| \frac{r_{pm} + r_{ma} e^{2ik_{zm}d}}{1 + r_{pm}r_{ma} e^{2ik_{zm}d}} \right|^2. \quad (5.5)$$

The ATR experiments were made by using the setup described in Sec. 4.1. The experiments were made on two different samples; a goldfilm of thickness 42 nm and a goldfilm of thickness 60 nm. They will be referred to as sample one and sample two. The films were fabricated in a sputtercoater aiming for a thickness of 40 nm and 60 nm. After the goldfilms were deposited,

the obtained thicknesses of sample one and two were measured with a profiler to 42 nm and 60 nm respectively. Eqn. 5.5 was fitted to the data obtained through these experiments by using a Matlab routine. The results of this fit are shown in Fig. 5.2 where the blue points are data from the experiments and the red line is the fit. In Tbl. 5.1 the fitting results and the measured parameters for the two samples are listed. When no data is available “NA” is written and when no remarkable difference between the measured and the calculated result is present, “same” is written.

By fitting Eqn. 5.5 to the data obtained from the experiments seen on Fig. 5.2, Matlab suggests a film thickness that in both samples is $\approx 30\%$ higher than the measured thickness. In Sec. 2.1.4, the effect of varying the thickness of the metal layer is demonstrated. When the thickness is changed from the ideal thickness, where the reflection intensity equals zero, holding other parameters constant, the minimum of reflection intensity is increased and the resonance angle is changed. When comparing the minimum reflection intensity of the two samples there is an observable difference. At the resonance angle the reflection intensity for Sample 1 decreases by a factor of 8 while the reflection intensity for sample two only decreases by a factor of 2.5. The minimum reflection intensity of sample one is 1.01 compared to sample two with 3.91. This indicates that the thickness of the metal film of sample one is closest to the ideal thickness. The resonance angles for the samples change as well. Thus, as demonstrated in Sec. 2.1.4 when the thickness is increased the resonance angle should be displaced toward a smaller angle. By changing the thickness from 40 nm to 60 nm, keeping other parameters constant, the resonance angle should be displaced by 0.35° towards a smaller angle according to theory. This is also the case for both the measured data and the fitted result. The difference between sample one and sample two is a change in resonance angle, toward a smaller angle, of $\approx 0.2^\circ$ close to that predicted by theory. One should notice that since the metal films on the two samples are not identical it is not only the thickness of the film that differs between sample one and sample two. As it appears from Tbl. 5.1 the permittivity of the two samples differs as well. Therefore it is not possible to compare the two samples directly.

The permittivity obtained from the fit equals for sample one $\varepsilon_m = -10.45 + i1.783$ and for sample two $\varepsilon_m = -8.328 + i1.161$. This seems reasonable compared to the value $\varepsilon_{\text{gold}} = -9.89 + i1.05$ obtained from [Palik, Emty]. The value of the real part of this permittivity is between the two values determined through the fit, while the imaginary part is lower than both of the values from the fit. This implies an increased damping in the metal film of both sample one and two, highest in the film of sample one.

For sample one, both the fitted angle of TIR and the resonance angle is comparable to the achieved data. This is not the case for sample two though. Here the fitted and measured resonance angles are consistent, but the angle of TIR differs by $\approx 1^\circ$. The “sharpness” of the resonance is measured here as a FWHM. Sample two has the sharpest resonance, $\approx 0.5^\circ$ thinner than sample one. This is as predicted by theory since a thicker metal film produces a sharper resonance. This is seen on Fig. 2.5.

5.2 LRM Results

In this section the images obtained in the LRM experiments are presented and discussed. To examine the dependence of different parameters involved in the experiments on the SPP properties a series of experiments was carried out. The parameters in the experiments were

- The laser excitation wavelength

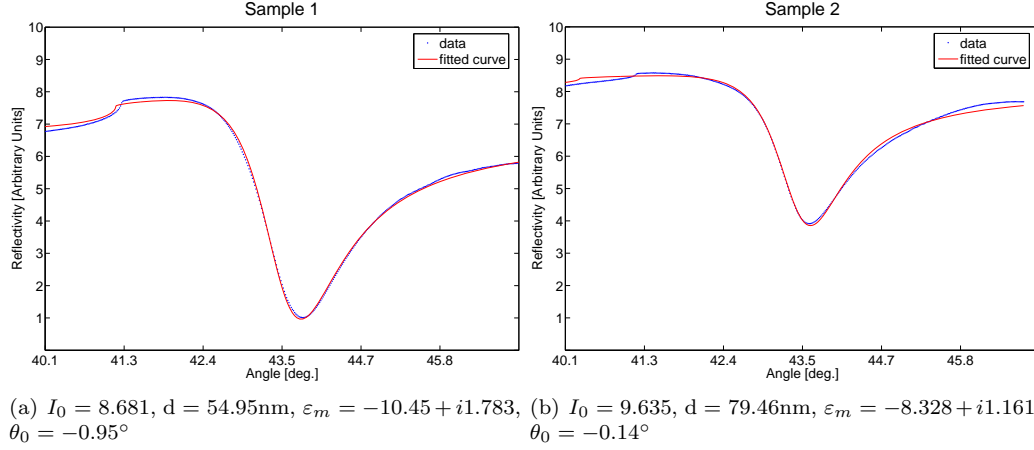


Figure 5.2: Plot of the reflection intensity curve for (a) sample one and (b) sample two. The blue points are the experimental data and the red line is the fit obtained by fresnel theory.

	Sample 1		Sample 2	
	Measured	Calculated	Measured	Calculated
Thickness	42nm	54.95nm	60nm	79,46 nm
SPP Resonance Pos.	43.84°	43.83°	43,645°	43.665°
TIR Pos.	41.31°	41.12°	41.22°	40,31°
FWHM	2.8°	Same	2,306°	Same
Permittivity of Metal	NA	-10.45+i1.783	NA	-8.328+i1.161
Minimum Refl. Int	1.01	Same	3.91	Same
Maximum Refl. Int	7.83	Same	8.57	Same
Refl. Int Difference	6.82	Same	4.66	Same
Angular Offset Error	NA	-0.95°	NA	-0.14°

Table 5.1: Compilation of experimental and fitted results for sample one and sample two. Refl. Int. means reflection intensity.

- The spacing between the nanoparticles in the chain
- The width of the chain

In Fig. 5.3 the images obtained from three different parabolas all with a center to center distance between the nanoparticles of 281 nm are shown. The images obtained from parabolas with a center to center distance between the particles of 322 nm are shown in Fig. 5.4. The images are arranged in the same way as the corresponding numerical simulations in Fig. 3.5 and Fig. 3.6. In all images the parabola height is 50 μm .

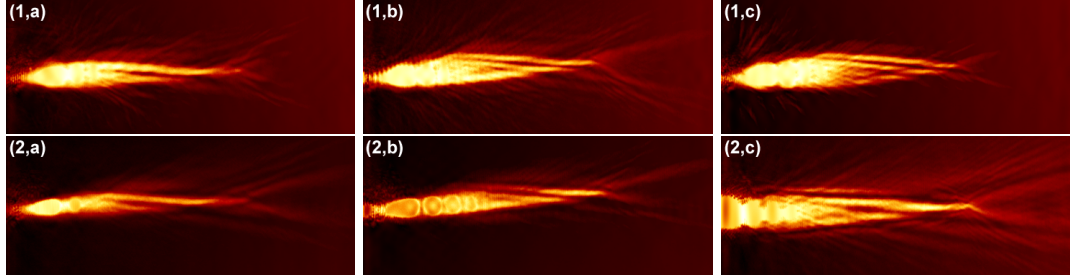


Figure 5.3: Leakage radiation microscopy pictures of SPPs propagating towards parabolic nanoparticle structures with a center to center distance of 281 nm. In all rows the columns represent parabolas (a), (b) and (c) as shown. In row one the laser excitation wavelength is 750 nm while in row two it is 855 nm.

5.2.1 Propagation Length

When comparing row one with row two on both Fig. 5.3 and 5.4 it is seen that the propagation length is longer in row 2 where the laser excitation wavelength is 855 nm. This is in accordance with the equation derived in the theory chapter, Eqn. 2.37, which states that the propagation length is proportional to the excitation wavelength. Thus, one should be careful when comparing two images directly since the contrast on the different images is not exactly the same. When comparing two images of different contrast one might get the false impression that the propagation length in one image is longer than in the other image. To minimize this error the contrast level of the CCD camera used to record the images was held on a nearly

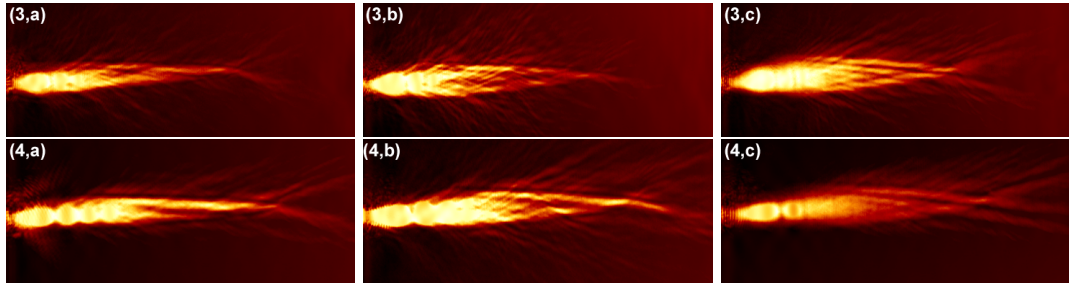


Figure 5.4: Leakage radiation microscopy pictures of SPPs propagating towards parabolic nanoparticle structures with a center to center distance of 322 nm. In all rows the columns represent parabolas (a), (b) and (c) as shown. In row one the laser excitation wavelength is 750 nm while in row two it is 855 nm.

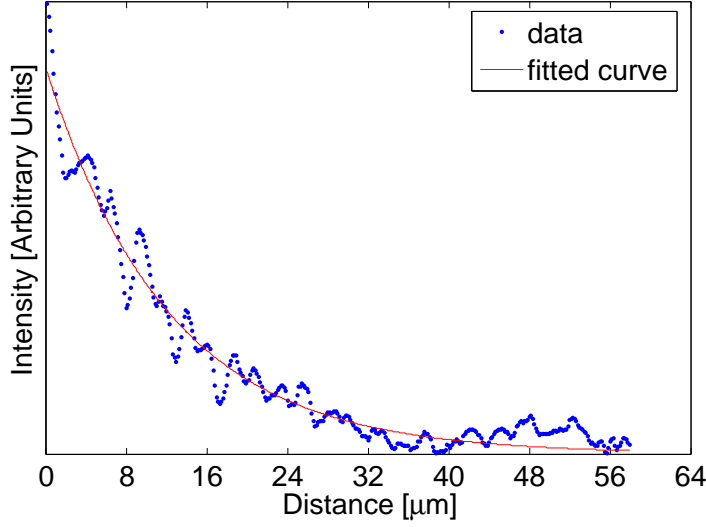


Figure 5.5: Intensity of SPP field plotted as a function of distance from excitation position. The blue points are data points measured from an LRM image of an SPP excited by EM radiation with a wavelength of 855 nm. The red curve shows a fit with an exponential form.

constant level. It was not possible to keep it on the exact same level, since it was necessary to fine tune the CCD camera in every experiment to visualize details as the interference fringes inside the parabolas. With this in mind and in spite of the small variation in contrast level it should still be valid to compare the propagation length as done above.

The SPP field intensity measured from an LRM image is plotted as a function of the distance from the point of excitation in Fig. 5.5. Each data point is the average pixel value of a line normal to the propagation direction. By fitting an exponential decaying function to this data it is possible to compare the SPP propagation length with theory. From Eqn. 2.37 the propagation length is calculated to $37.9 \mu\text{m}$, by using $\varepsilon_m = -28 + i1.8$ from [Palik, Emty] and $\lambda = 855 \text{ nm}$. From the fitted curve in Fig. 5.5 the propagation length is found to be $12.3 \mu\text{m}$. Thus, the real propagation length is in this case a third of the length predicted by theory. It is a possibility that defects in the surface of the sample will scatter the excited SPP causing further intensity decay in the propagation direction than that predicted by theory.

5.2.2 Parabola Shape and Particle Spacing

In the images there is seen clear difference between parabolas of different widths. Generally the (c) parabolas give better images than parabolas of smaller width. In the (c) parabolas interference fringes are observed inside the parabola. This interference is also seen in the numerical simulations and is believed to be due to interference between the incident SPP beam and the beam reflected from the branches of the parabola. The focusing properties of the parabola are more easily seen in the wide parabolas because the beam diverges more before being reflected.

In the parabolas of small width the SPP beam seems to be split in two on the right side of the parabola. This is most easily seen in image (4,c). This suggest that parabolic structures of small width can be used as beamsplitters.

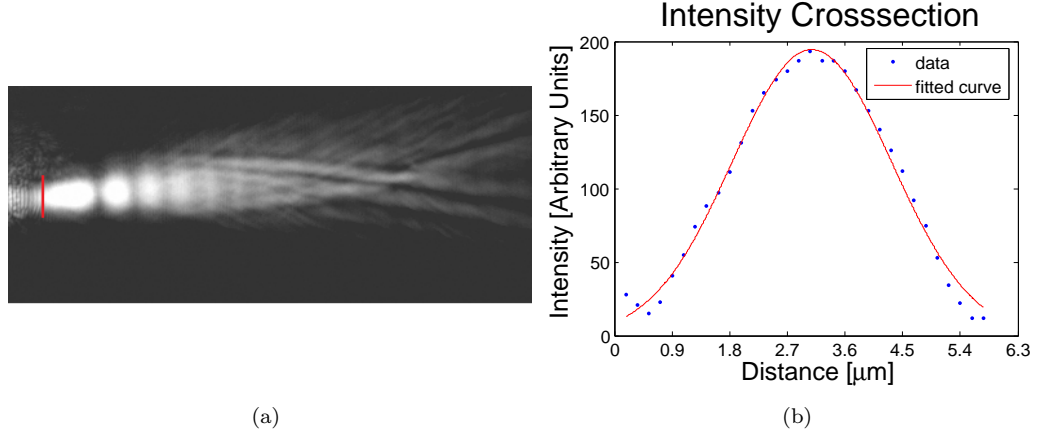


Figure 5.6: (a) shows an LRM image of an SPP scattered by a parabola of nanoparticles. The red line indicates the position of the measured intensity distribution shown on (b). Here the blue points are the intensity measured along the red line on (a) while the red curve is a gaussian fit.

As for the spacing between the nanoparticles there does not seem to be much difference between the images obtained from parabolas with 322 nm spacing and those obtained with 281 nm spacing. This is consistent with the numerical results.

5.2.3 Shape of the SPP Beam

In the simulations, the incoming SPP was modelled by a divergent gaussian beam. For the simulations to be valid and be consistent with the experiments, the SPPs excited in the experiments should have the same intensity profile. In Fig. 5.6 an LRM image of an SPP incident on a parabola of nanoparticles is shown together with a plot of the intensity distribution perpendicular to the propagation direction. The blue points on Fig. 5.6(b) are the data measured along the red line on Fig. 5.6(a) while the red curve is a gaussian fit of the data points. By comparing the data points and the gaussian fit on Fig. 5.6(b) it is seen that the SPP intensity distribution fits a gaussian shape with good agreement. In the simulations the initial SPP beam diameter was set to 3 μm . From the gaussian fit in Fig. 5.6(b) the beam diameter is calculated to 3.5 μm . This is in good agreement with the simulations. It is not possible to measure the SPP beam diameter directly at the point of excitation so the diameter is measured after the beam has propagated a small distance and therefore has diverged.

5.2.4 Comparison Between Numerical Results and Experiments

In Fig. 5.7 the experimental image (4,c) is shown along with the numerical simulation of the same image. Most of the experimental features are reproduced in the simulation. The interference seen in the simulation is also present in the experimental image, although it is not as distinct as in the simulation. On the right hand side of the parabola there is good correspondence. The simulation does also correctly predict the leakage of SPP radiation through the parabola branches. Unfortunately it seems that the parabola was not illuminated symmetrically which is why the leakage through the upper parabola branch is larger than the leakage through the lower branch. It should be noted that the contrast of the simulated image has

been changed to reflect the nonlinearity of the CCD camera used to capture the experimental images, so that the two can be more easily compared.

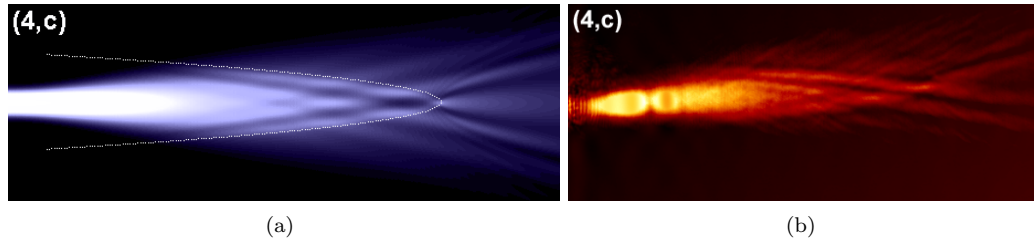


Figure 5.7: Comparison between the experimentally obtained and the numerically obtained image (4,c).

Chapter 6

Conclusion

In this project excitation and scattering of SPPs have been treated theoretically and experimentally. The conditions for excitation of SPPs and the propagation of SPPs through different structures have been investigated. Two theoretical models for simulation of SPP scattering have been made, a scalar model and a vectorial model, and the conditions for correspondence between the two models have been established. For the scalar model to be valid the x-component of the field has to be negligible compared to the z-component and it was found that in this limit the two models are connected by the polarizability Eqn. 2.85.

On the experimental side excitation of SPPs in the Kretschmann-Raether configuration have been tried out using gold films. Two different film thicknesses were used, 42 nm and 60 nm. It was found that the reflection intensity can be very well described using Fresnel theory. Using Fresnel theory the conditions for minimum reflection intensity was derived.

Propagation of SPPs through parabolic structures of nanoparticles has been investigated both theoretically and experimentally. It has been shown that the parabolas can be used to focus SPPs and that parabolas of small width could have potential as beam splitters. The experimentally obtained results were compared to the theoretically obtained results and it was shown that the model corresponds well to the experiments.

Appendix A

Surface Plasmon Excitation

A.1

The relationship between the x and z-component of the amplitude of the electric field in both medium 1 and medium 2 is here calculated utilizing Maxwell's equation, $\nabla \cdot \mathbf{E} = 0$. The fields are given by Eqn. 2.1 and 2.3. Both the electric field in medium 1 and 2 only oscillates in the xz-plane. Maxwell's equation for the field in medium 1 yield

$$\frac{\partial E_{x1}}{\partial x} + \frac{\partial E_{z1}}{\partial z} = 0. \quad (\text{A.1})$$

By inserting the derivatives of the x and z components of the field the following is found

$$ik_x E_{x1} e^{i(k_x x - \omega t)} e^{ik_{z1} z} + ik_{z1} E_{z1} e^{i(k_{x1} x - \omega t)} e^{ik_{z1} z} = 0 \quad (\text{A.2})$$

$$k_x E_{x1} = -k_{z1} E_{z1} \quad (\text{A.3})$$

$$E_{z1} = -E_{x1} \frac{k_x}{k_{z1}}. \quad (\text{A.4})$$

An exact similar calculation can be performed for the field in medium 2.

A.2

The relationship between the y-component of the amplitude of the magnetic field and the x-component of the amplitude of the electric field is here calculated using Faraday's law $\nabla \times \mathbf{E} = -\mu \frac{\partial \mathbf{H}}{\partial t}$. The fields are given by Eqn. 2.1 to 2.4. In this appendix only the fields in medium 1 are considered. First the curl of the electric field is determined

$$\nabla \times \mathbf{E} = \hat{\mathbf{i}} \left(\frac{\partial}{\partial y} E_z - \frac{\partial}{\partial z} E_y \right) - \hat{\mathbf{j}} \left(\frac{\partial}{\partial x} E_z - \frac{\partial}{\partial z} E_x \right) + \hat{\mathbf{k}} \left(\frac{\partial}{\partial x} E_y - \frac{\partial}{\partial y} E_x \right). \quad (\text{A.5})$$

Since the y-component of the electric field, E_y , is zero and the x and z-components, E_x and E_z , has not got any y-dependency the first and last term in Eqn. A.5 equals zero. By inserting the derivatives of the field into the term left in Eqn. A.5 the curl equals

$$\nabla \times \mathbf{E} = \hat{\mathbf{j}} \left(ik_{z1} E_{x1} e^{i(k_x x - \omega t)} e^{ik_{z1} z} - ik_x E_{z1} e^{i(k_x x - \omega t)} e^{ik_{z1} z} \right). \quad (\text{A.6})$$

Turning to the right hand side of Faraday's law, the derivative of \mathbf{H} with respect to t has to be calculated. This equals

$$\frac{\partial \mathbf{H}}{\partial t} = \hat{\mathbf{j}} \left(-i\omega H_y e^{i(k_x x - \omega t)} e^{ik_{z1} z} \right). \quad (\text{A.7})$$

Inserting Eqn. A.6 and A.7 into Faraday's law yields the equation

$$ik_{z1} E_{x1} e^{i(k_x x - \omega t)} e^{ik_{z1} z} - ik_x E_{z1} e^{i(k_x x - \omega t)} e^{ik_{z1} z} = \mu\mu_0 i\omega H_y e^{i(k_x x - \omega t)} e^{ik_{z1} z}, \quad (\text{A.8})$$

where the permeability μ has been inserted as $\mu\mu_0$ and μ is the relative permeability, and the unit vectors $\hat{\mathbf{j}}$ has cancelled out. Now the exponentials and the complex i cancel out yielding the simple expression

$$E_{x1} k_{z1} - E_{z1} k_x = \mu\mu_0 \omega H_{y1}. \quad (\text{A.9})$$

By inserting Eqn. 2.10 this yields

$$E_{x1} k_{z1} + E_{x1} \frac{k_x^2}{k_{z1}} = \mu\mu_0 \omega H_{y1} \quad (\text{A.10})$$

$$E_{x1} \frac{k_{z1}^2 + k_x^2}{k_{z1}} = \mu\mu_0 \omega H_{y1}. \quad (\text{A.11})$$

The numerator in the left hand side of Eqn. A.11 is $k_{z1}^2 + k_x^2 = k_1^2 = k^2 n_1^2 = n_1^2 \omega^2 / c^2$, where k is the free space wave vector and n_1 is the refractive index of medium 1. This gives therefore

$$E_{x1} \frac{\omega^2 n_1^2}{c^2 k_{z1}} = \mu\mu_0 \omega H_{y1}. \quad (\text{A.12})$$

The speed of light in medium 1 is given as $c = n_1^2 / \sqrt{\mu\mu_0 \epsilon\epsilon_0}$. By inserting this into Eqn. A.12 the relationship between the y-component of the amplitude of the magnetic field and the x-component of the amplitude of the electric field is found as

$$E_{x1} \frac{\omega \epsilon \epsilon_0}{k_{z1}} = H_{y1}. \quad (\text{A.13})$$

The calculations can be carried out in exactly the same manor for the fields in medium 2.

Appendix B

Reflectivity of a two interface system

The total reflection coefficient of an incoming light beam on a two interface system is here derived as the sum of individual reflectivity coefficients from each reflected wave. The system considered is a prism/metal/air system as depicted on Fig. B.1. When light impinges on the prism/metal interface from the prism side, it is partially reflected and partially transmitted. The transmitted part is further reflected back on the metal/air interface as seen on Fig. B.1 and then transmitted at the metal/prism interface. At this point it has suffered a phase change of $\Delta\phi = 2k_z d$, since the path length in the z-direction is twice the thickness of the metal layer. The total reflection coefficient becomes

$$\begin{aligned} r &= r_{12} + t_{12}r_{23}t_{21}e^{i\Delta\phi} + t_{12}r_{23}e^{i\Delta\phi}r_{21}r_{23}t_{21}e^{i\Delta\phi} + \\ &\quad t_{12}r_{23}e^{i\Delta\phi}r_{21}r_{23}e^{i\Delta\phi}r_{21}r_{23}t_{21}e^{i\Delta\phi} + \dots \\ &= r_{12} + t_{12}r_{23}t_{21}e^{i\Delta\phi} \left(1 + r_{21}r_{23}e^{i\Delta\phi} + (r_{21}r_{23}e^{i\Delta\phi})^2 + \dots \right). \end{aligned} \quad (\text{B.1})$$

Remembering that for $|x| < 1$,

$$1 + x + x^2 + \dots = \frac{1}{1 - x},$$

Eqn. B.1 can be rewritten as

$$r = r_{12} + \frac{t_{12}r_{23}t_{21}e^{i\Delta\phi}}{1 - r_{21}r_{23}e^{i\Delta\phi}}. \quad (\text{B.2})$$

Knowing that $t_{ij} = 1 + r_{ij}$ and $r_{ij} = -r_{ji}$, the product $t_{12}t_{21}$ in the nominator of Eqn. B.2 can be written as

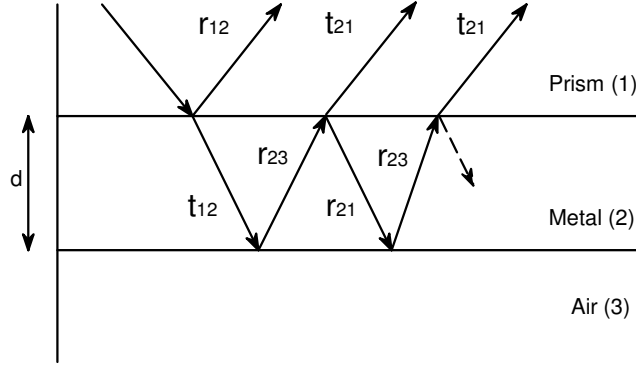


Figure B.1: Multiple reflections in the metal layer

$$\begin{aligned}
 t_{12}t_{21} &= (1 + r_{12})(1 + r_{21}) \\
 &\quad (1 + r_{12})(1 - r_{12}) \\
 1 - r_{12} + r_{12} - r_{12}^2 &= 1 - r_{12}^2.
 \end{aligned}$$

By inserting this in Eqn. B.2 the total reflection coefficient can be expressed without the transmission coefficient as

$$r = \frac{r_{12} - r_{12}r_{21}r_{23}e^{i\Delta\phi} + r_{23}e^{i\Delta\phi} + r_{23}r_{12}r_{21}e^{i\Delta\phi}}{1 - r_{21}r_{23}e^{i\Delta\phi}} \quad (\text{B.3})$$

$$= \frac{r_{12} + r_{23}e^{i\Delta\phi}}{1 + r_{12}r_{23}e^{i\Delta\phi}}. \quad (\text{B.4})$$

The total reflectivity of the two interface system can now be expressed as

$$R = \left| \frac{E_r}{E_{in}} \right| = |r|^2 = \left| \frac{r_{12} + r_{23}e^{i\Delta\phi}}{1 + r_{12}r_{23}e^{i\Delta\phi}} \right|^2. \quad (\text{B.5})$$

Bibliography

- [Barnes et al., 2003] Barnes, W. L., Deroux, A., and Ebbesen, T. W. (2003). Surface plasmon subwavelength optics. *Nature*, 424:824–830.
- [Bouhelier et al., 2001] Bouhelier, A., Huser, T., Tamaru, H., Güntherodt, H.-J., and Pohl, D. (2001). Plasmon optics of structured silver films. *Physical Review B*, 63.
- [Bozhevolnyi and Coello, 1998] Bozhevolnyi, S. I. and Coello, V. (1998). Elastic scattering of surface plasmon polaritons: Modelling and experiment. *Physical Review B*, 58:10899–10910.
- [Brongersma, 2007] Brongersma, M. (26/11-2007). Engineers study whether plasmonics, “light on a wire”, is circuitry wave of future. <http://news-service.stanford.edu/news/2005/march16/plasmon-031605.html>.
- [Drezet et al., 2006] Drezet, A., Hohenau, A., Stepanov, A. L., Ditlbacher, H., Steinberger, B., Galler, N., Aussenegg, F. R., Leitner, A., and Krenn, J. R. (2006). How to erase surface plasmon fringes. *Applied Physics Letters*, 89:91117.
- [Evlyukhin and Bozhevolnyi, 2005] Evlyukhin, A. B. and Bozhevolnyi, S. I. (2005). Point-dipole approximation for surface plasmon polariton scattering: Implications and limitations. *Physical Review B*, 71:134304.
- [Evlyukhin et al., 2006] Evlyukhin, A. B., Bozhevolnyi, S. I., Stepanov, A. L., and Krenn, J. R. (2006). Splitting of a surface plasmon polariton beam by chains of nanoparticles. *Applied Physics B*, 84:29–34.
- [Keller et al., 1992] Keller, O., Xiao, M., and Bozhevolnyi, S. (1992). Configurational resonances in optical near-field microscopy: a rigorous point dipole approach. *Surface Science*, 280:217–230.
- [Kretschmann and Raether, 1968] Kretschmann, E. and Raether, H. (1968). Radiative decay of nonradiative surface plasmons excited by light. *Naturforsch. AZ. Naturforsch*, 23:2135–2136.
- [Otto, 1968] Otto, A. (1968). Excitation of nonradiative surface plasma waves in silver by the method of frustrated total reflection. *Z. Phys.*, 216:398–410.
- [Palik, Emty] Palik, E. D. (Emty). *Optical Constants of Metals*. Emty.
- [Petersen et al., 2006] Petersen, R., Andersen, O. Z., Larsen, T., and Kildeby, N. L. (2006). *Immobilization of Cutinase on Nanoparticles*. University of Aalborg.

BIBLIOGRAPHY

- [Radko et al., 2007] Radko, I. P., Bozhevolnyi, S. I., Evlyukhin, A. B., and Boltasseva, A. (2007). Surface plasmon polariton beam focusing with parabolic nanoparticle chains. *Optics Express*, 15:6576.
- [Raether, 1986] Raether, H. (1986). *Surface Plasmons*. Springer-Verlag.
- [Sambles et al., 1991] Sambles, J. R., Bradbery, G. W., and Yang, F. (1991). Optical excitation of surface plasmons: an introduction. *Contemporary Physics*, 32:173–183.